Benchmarking of the NACA 63_3-018 Trailing-Edge Noise in a Broad Reynolds Number Range as Part of the IEA Task 39

Guillem Vergés i Plaza*
Technical University of Denmark, Frederiksborgvej 399, 4000, Roskilde, Denmark
Flow Physics and Technology Department, Delft University of Technology, 2629 HS Delft, The Netherlands

Andreas Fischer†, Oliver Lylloff‡, Christian Bak§, Anders S. Olsen¶, Franck Bertagnolio‖
Technical University of Denmark, Frederiksborgvej 399, 4000, Roskilde, Denmark

Salil Luesutthiviboon**, Tercio Lima Pereira††, Daniele Ragni‡‡, Francesco Avallone§§
Flow Physics and Technology Department, Delft University of Technology, 2629 HS Delft, The Netherlands

Alexandre Suryadi¶¶, Michaela Herr***
German Aerospace Center (DLR), Lilienthalplatz 7, 38108 Braunschweig, Germany

An experimental aero-acoustic characterisation of the NACA 63_3-018 airfoil is presented in this study, featuring trailing-edge noise emissions with and without serrations. Measurements have been carried out for a chord-based Reynolds number range between 0.18×10^6 and 4.8×10^6. Two airfoil models with different chord lengths have been tested in five different wind tunnels. The goal is to compare the measurements in different facilities, quantify the uncertainties, and establish a validation database that can serve as a benchmark for computational studies. The tests have been performed with clean and forced-transition boundary layers for a variety of angles of attack. The effect on the spectral slope and peak levels is evaluated. Scaling laws have been applied to compare different test conditions. The quality and nature of the collapse, as well as the applicability limits of the scaling, are examined. Different serration geometries have been tested at different flap angles. The noise reduction dependence on the aerodynamic loading is discussed. This work is based on an initiative of Task 39 "Quiet Wind Turbine Technology" of the Technology Collaboration Programme (TCP) of the International Energy Agency (IEA).

Nomenclature

α_{eff}	=	effective angle of attack (deg)
α_{geo}	=	geometrical angle of attack (deg)
b	=	span width (m)
c	=	chord length (m)
C_d	=	drag coefficient (-)
C_l	=	lift coefficient (-)
C_p	=	pressure coefficient (-)
δ^*	=	displacement thickness, subscript may indicate pressure side ($_{PS}$) or suction side ($_{SS}$) (m)

*MSc Student, European Wind Energy Master - Rotor Design - Aerodynamics, E-mail: guillem.verges@gmail.com
†Senior Researcher, Department of Wind and Energy Systems, E–mail: asfi@dtu.dk
‡Postdoc, Department of Wind and Energy Systems, E–mail: ollyl@dtu.dk
§Professor, Department of Wind and Energy Systems, E–mail: chba@dtu.dk
¶Senior Development Engineer, Department of Wind and Energy Systems, E–mail: sols@dtu.dk
‖Senior Researcher, Department of Wind and Energy Systems, E–mail: frba@dtu.dk
**PhD Candidate, Section Aircraft Noise Climate Effect, E–mail: s.luesutthiviboon@tudelft.nl
††PhD Candidate, Section Wind Energy, E–mail: l.t.limapereira@tudelft.nl
‡‡Associate Professor, Section Wind Energy, E–mail: d.ragni@tudelft.nl
§§Assistant Professor, Section Wind Energy, E–mail: f.avallone@tudelft.nl
¶¶Research Engineer, Dept. of Wind Energy, Institute of Aerodynamics and Flow Technology, E-mail: alexandre.suryadi@dlr.de,
***Head of Wind Energy Department, Institute of Aerodynamics and Flow Technology, E-mail: michaela.herr@dlr.de

f	=	frequency (Hz)
t_{TE}	=	trailing-edge thickness (m)
M_U	=	wind tunnel free-stream velocity based Mach number (-)
$OSPL_{1/n}$	=	overall sound pressure level calculated from 1/n octave band spectrum (dB)
PSD	=	far-field noise power spectral density (dB/Hz)
r	=	distance between the observer and the sound source (m)
Re_c	=	chord-based Reynolds number (-)
$SPL_{1/n}$	=	1/n octave band sound pressure level (dB)
$SPL_{1/n,scaled}$	=	scaled 1/n octave band sound pressure level (dB)
$\Delta SPL_{1/n}$	=	noise reduction based on 1/n octave band sound pressure level (dB)
St_ℓ	=	Strouhal number based on characteristic length ℓ (-)
U	=	wind tunnel free-stream velocity (m/s)
X, Y, Z	=	chordwise, vertical, and spanwise coordinates from the TE (Fig. 1) (m)

I. Introduction

Trailing-edge (TE) noise arises from the interaction of the turbulent boundary layer, and the pressure fluctuations that it generates in the surface, with the trailing edge [1, 2]. It has been identified as a primary noise source for wind turbines [3]. It is thus of industrial interest to predict and mitigate its impact, an example of this is the Task 39 of the International Energy Agency Wind Technology Collaboration Programme (IEA Wind TCP Task 39). Its goal is to accelerate the development and deployment of quiet wind turbine technology by providing supporting research database as the foundation for establishing international standards and governmental regulations. The task addresses the engineering questions of wind turbine noise generation, reduction, and propagation, and the socio-psychological questions of the wind turbine noise impact to health, well-being and consent and other non-noise factors. An interdisciplinary work group is also established to disseminate the interaction between engineering and socio-psychological sciences.

The goal of this collaborative paper is to create a high quality and comparable database of trailing-edge noise from both straight and serrated TEs. A very related effort in the same direction is the Benchmark problems for Airframe Noise Computations (BANC) workshop (category I, TE noise), a series of workshops which aim to cross-check available measurement data with different computation methods [4–6]. The experimental data-sets available so far were composed of a symmetric NACA 0012, a cambered DU96–W180, and a NACA 64-618 airfoils without serrations in a Re_c range from 1×10^6 to 1.5×10^6. This Reynolds range, however, is lower than the one that modern wind turbines work at. It is also desirable to characterise the error bars and understand the uncertainty in the measurements carried out with different models and in different facilities. Additionally, serrations have become largely used to reduce the trailing-edge noise of wind turbines [7], and experimental data is required to validate new noise models (e.g. [8]). Therefore, it is of high interest to include serrations into the data-base.

These gaps were partially tackled in the study of Ferret Gasch et al. [9] where two Siemens-Gamesa cambered airfoils were tested to a maximum Re_c of 3.7×10^6. These results were used to blindly test the accuracy of different noise prediction codes. The recommendations of such study insisted again in the need of carrying out uncertainty quantification of the measurements and improve the validation database specially at moderate to high Reynolds numbers.

The leading aero-acoustic facilities in Europe have carried out cross-facility aero-acoustic tests of a NACA 63_3-018 airfoil as the first collaborative step to establish the database as well as to quantify the uncertainty. This airfoil has been selected because its symmetry helps to accurately determine the zero angle of attack, but when placed at different α the resulting pressure distributions are similar to those commonly found in wind turbines (e.g. [10]). In order to cover the largest Re_c possible, two models have been built: a large one (subsequently called *HRM*: High Reynolds number Model), with 0.9 m chord, and a small one (*LRM*: Low Reynolds number Model) with a chord of 0.2 m. The HRM has been tested in the Poul La Cour Tunnel (PLCT) at the Denmark Technical University (DTU), and the LRM has been studied in both the A-Tunnel at TU Delft, and the Acoustic Wind Tunnel Braunschweig (AWB) in the German Aerospace Center (DLR). The aerodynamics of the HRM have also been measured in the low-speed Wind-Tunnel Braunschweig (NWB) of the German-Dutch Wind Tunnels Foundation (DNW) and in the Low-Turbulence Tunnel (LTT) of TU Delft.

This paper presents preliminary comparisons of test results from the aforementioned facilities. This paper is structured as follows. A description of the model and serration geometries is given in Section II, followed by a summary of the facilities set-up in Section III. The aerodynamic results are then analysed in Section IV, succeeded by the study of the acoustic results with straight trailing edge in Section V. Finally, the effect of the serrations is discussed in Section VI.

II. Model Description

Two NACA 63_3-018 airfoils (Fig. 1) were built for this study, namely the Low Reynolds number Model (LRM) and the High Reynolds number Model (HRM). They have a chord length of 0.2 m and 0.9 m respectively. The base span width is 0.4 m for the LRM and 1.816 m for the HRM, and modular extensions were also built to adapt the models to the specific heights of the wind tunnel test sections. The LRM span width was 0.4 m when tested in the A-Tunnel, and 0.8 m in the AWB. For the HRM, these values were 1.25 m in the LTT, 2 m in the PLCT (DTU), and 2.8 m in the NWB. The HRM was made of sheet metal skins over rib and stringer structures. The LRM was manufactured as an assembly of three solid modular aluminium structures. More details about the models may be found in [11, 12]. The trailing edge thickness is $t_{TE} = 7.5c \times 10^{-4}$ for both models.

The HRM is equipped with 192 surface pressure tabs. They are organised in 7 rows in order to characterise the flow three-dimensionality. The main row, in the middle of the model, has higher density with 96 tabs. They have an offset in the spanwise direction to minimise interferences. In the LTT, since the base span of the model could not fit completely in the test section, this mid row was not fully centered. It was located around $1c$ (0.9 m) from the bottom wall instead. The LRM has 28 pressure tabs in the middle of the span with an spanwise angle of 15 deg.

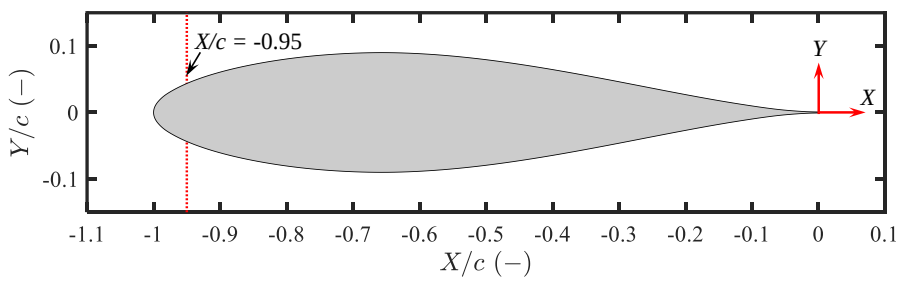

Fig. 1 NACA 63_3-018 airfoil with tripping location and axis orientations.

The measurements have been carried out with both clean and tripped boundary layer. The forced transitions helps with the comparability of the results, and supports the reproducibility of the measurements. For the tripped boundary layer case, zig-zag strips have been employed at $X = -0.95c$ on both sides of the airfoil. For the LRM a thickness of 0.5 mm, a width of 6 mm, and an angle of 70 deg. have been used. For the HRM these values are 0.4 mm, 12 mm, and 60 deg. respectively. The HRM tripping was applied with a base tape of 0.06 mm thickness (Fig. 7).

Different trailing-edge serrations have been tested. Two geometries have been selected: sawtooth and iron serrations, illustrated in Fig. 2. The geometries are taken from a numerical investigation of Avallone et al. [13], which compared the iron serrations to the conventional sawtooth ones, and found increased noise reduction in the former. This was attributed to decreased scatter in the serration roots. The serrations' wavelength is $0.05c$, and the peak amplitude is $0.1c$. Both types have been installed parallel to the chord ($\varphi = 0$ deg), and the sawtooth serrations have also been tested at $\varphi = 8$ deg for the LRM and $\varphi = 4$ deg for the HRM. Details about the installation procedure may be found in the work of Luesutthiviboon et al. [11]. There is significant uncertainty in the flap angle of the serrations. This has been measured in the serrations tested by DTU, where important deviations from the nominal values were detected. The iron and sawtooth serrations which should have been placed at $\varphi = 0$ deg were measured to be at 4.16 deg and 4.43 deg respectively. Moreover, spanwise differences up to 3.8 deg were also found. For the flapped case at nominal $\varphi = 4$ deg. the real value (spanwise averaged) was 9.39 deg.

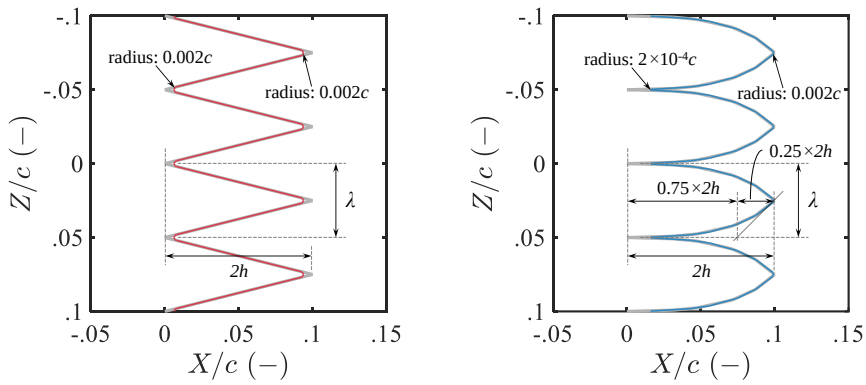

(a) Sawtooth serrations **(b) Iron serrations**

Fig. 2 Drawings of the trailing-edge serrations used on the airfoil. In gray, the geometry used in the study of Avallone et al. [13].

III. Facilities Description

A. The PLCT at DTU

The Poul La Cour Wind Tunnel is a closed loop return wind tunnel (Fig. 3). The airline is 66 m long and 27 m wide (furthest separated points of the airline tube, but neglecting the wind tunnel buildings). The air volume inside the airline is about 3875 m^3. The whole airline is built in concrete because of acoustic considerations. The fan of the wind tunnel is driven by a 2.4 MW engine and has a diameter of 4.7 m. The fan was limited to 400 RPM or an engine power output of 1.8 MW, because the tunnel loss estimate proved to be too conservative. The fan can generate an air flow of up to 630 m^3/s at 400 RPM when a test object is placed in the tunnel.

The settling chamber has a cross section of 6 x 9 m and is equipped with a honeycomb and 3 mesh grids to rectify the flow and reduce turbulence before entering the test section. The mesh grid goes from a coarse to a fine mesh size. The grid size of the finest mesh is 0.2 mm. The flow is accelerated through a nozzle with a contraction ratio of 9:1 before entering the test section. The test section has a cross section of 2×3 m and is 9 m long. The top speed is 105 m/s and the turbulence intensity is below 0.1 %.

Measurements can be carried in a traditional hard-wall configuration [14] to focus on the aerodynamics, or in the acoustic configuration that is based on the new Kevlar wall technology [15]. The noise is measured by a phased array with 84 microphones of the type B&K type 4985 1/4". It is placed in the anechoic chamber with a distance of 1.2 m from the Kevlar wall, and it is centered above the trailing edge of the aerofoil and its mid-span. The microphone data was acquired with a B&K LAN-XI type 3053 system at a sample rate of 16384 Hz. The measurements have been post-processed using the deconvolution algorithm *CLEAN based on spatial coherence*, CLEAN-SC [16]. More information about the set-up and the post-processing may be found in O. Lylloff's PhD [17].

B. The A-Tunnel at TU Delft

At Delft University of Technology, the small NACA 63_3-018 was tested in the A-Tunnel, an open-jet anechoic vertical wind tunnel. Full description of the facilities and results to be further discussed in this paper have been presented in a publication of Luesutthiviboon et al. [11]. In the A-tunnel, a semi-open test section is placed in a room treated by acoustically absorbent foam wedges. Acoustic characterization of the A-Tunnel anechoic chamber including further extensive details can be found in a publication of Merino-Martinez et al. [18]. To achieve different free-stream velocity ranges, the test section can be placed on different outlet nozzles having different contraction ratios. Two different nozzles have been used for the measurements, one with a cross-section of 400×700 mm ($2c \times 3.5c$), which will be referred as *Large* or *TUD-A-L*, and one with a cross-section of 400×250 mm ($2c \times 1.25c$), which will be called *Small* or *TUD-A-S*. The Small nozzle allowed for a higher Re_c range, but its relatively smaller jet width limited the measurements to $\alpha = 0$ deg. A photograph of the TUD-A-L case in the A-Tunnel is shown in Fig. 4a. The full measurement envelope is presented in Fig. 13.

This paper presents both aerodynamic and acoustic data from the A-Tunnel. Static pressure distributions were

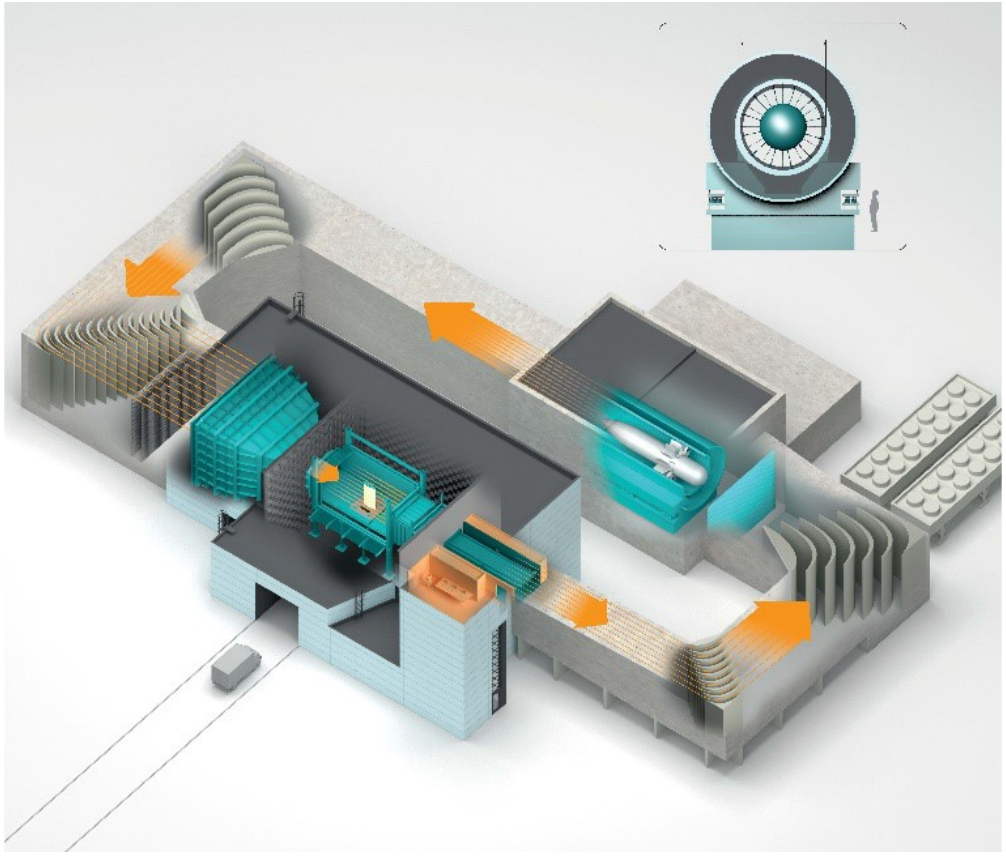

Fig. 3 The Poul La Cour Wind Tunnel.

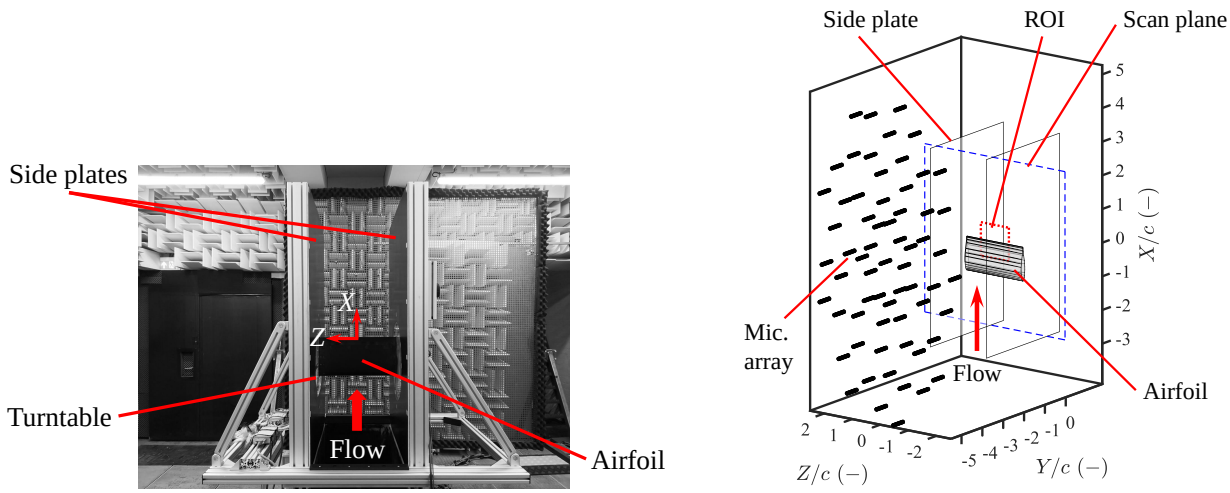

(a) **(b)**

Fig. 4 (a) The small NACA 63_3-018 airfoil in the A-Tunnel and (b) Schematic of the microphone array in the A-tunnel.

collected via Honeywell TruStability HSCDRRN025MDAA3 differential pressure transducers with a ±2.5 kPa range and ±6 Pa accuracy. Subsequently, the lift coefficients are calculated by a method described in Section IV.A.

The Hot-Wire Anemometry (HWA) Technique was employed to extract the boundary-layer velocity profiles at $X/c = -0.02$, i.e. close to the TE. Specifications of the HWA system can be found in the publication of Luesutthiviboon et al. [11].

The acoustic data was recorded using an array of 64 microphones and post-processed using conventional frequency-domain beamforming (CBF) [19]. The acoustic maps were then integrated using the Source Power Integration (SPI) technique. A schematic of the microphone array and the Region Of Integration (ROI) is shown in Fig. 4b. For more details about post-processing technique, the paper from Merino-Martinez [18] may be consulted.

C. The LTT at TU Delft

The large NACA 63_3-018 model was tested in the Low-Turbulence Tunnel (LTT) at TU Delft. The aforementioned publication of Luesutthiviboon et al. [11] also contains full details of the LTT facility, including aero-acoustic results.

The LTT is a closed-circuit wind tunnel originally designed for aerodynamic tests. The LTT has a contraction ratio of 17.8 and a turbulence intensity range between 0.015% and 0.07% for free-stream flow speeds between 20 and 70 m/s. The airfoil was installed in a specially-made test section, in which the wall panels are 'acoustically treated' by Kevlar-covered Melamine wedges.

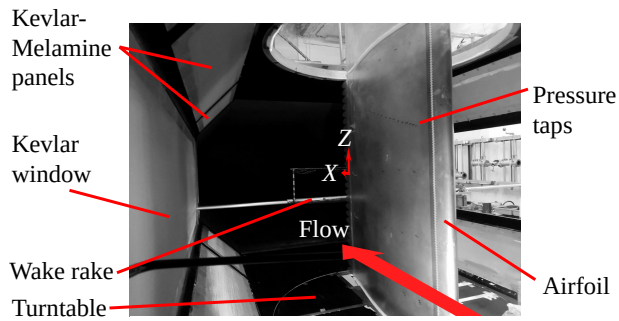

Fig. 5 The large NACA 63_3-018 airfoil in the LTT.

This paper only presents aerodynamic test results from the LTT, namely, the lift curves, and the boundary layer profiles. To read the static surface pressure data, the 101 pressure taps on the model were connected to a DTC pressure system with 6 ESP–HD scanners. The aerodynamic corrections for the LTT hard-wall test section can be found in the works of Timmer and Garner et al. [20, 21]. It has been confirmed by Luesutthiviboon et al. [11] that the pressure distribution and lift obtained in the acoustically test section do not deviate from that obtained in the hard-wall configuration. A brief comparison of both set-ups is also presented in this study.

Velocity fields at the TE region of the model were extracted by the Particle Image Velocimetry (PIV) technique. Specifications of the PIV setup can be found in the work of Luesutthiviboon et al. [11]. The edge of the boundary layer was defined where the spanwise vorticity is constant. Subsequently, the boundary layer integral parameters were extracted.

D. The AWB at DLR

The Acoustic Wind Tunnel Braunschweig (AWB) is an anechoic open-jet, closed-circuit wind tunnel operated by the German Aerospace Center (DLR - *Deutsches Zentrum für Luft- und Raumfahrt*), Braunschweig. The test section is treated with acoustic linings to reduce sound reflection in the test section. The nozzle cross-section is 0.8 m in width and 1.2 m in height, and the maximum wind speed at the nozzle is 65 m/s with a turbulence intensity of 0.3% [22]. The wind tunnel model is installed along the width of the nozzle via two side extensions of the nozzle (see Fig. 6). Two far field sound measurement systems were used extensively in the measurement campaign.

The directional microphone with a 1.4 m outer diameter elliptic reflector is placed along a motorized traversing system below and facing the model's pressure side. At the near-focal point of the elliptical reflector is a Brüel&Kjær 4136 1/4" microphone, which records the reflected noise. The distance between the microphone to the sound source (geometrically represented by the model's trailing edge) is approximately 1.15 m. Because the directional mirror's insensitivity to the distance to the sound source, its height with respect to the wind tunnel center line was not adjusted [23]. Assuming line sources, the noise was measured along a straight line cutting through the mid-span of the model.

Prior to the actual measurement, a scan along the streamwise axis was performed with the directional microphone to identify the leading-edge and trailing-edge noise distribution. Furthermore, because sound is convected with the free-stream and refracted by the wind tunnel's shear layer, the measured distribution is further downstream than the position of the model. The shifted position is predominantly dependent on the freestream velocity. The result of the scan shows that each noise source has a distinct distribution, so trailing-edge noise measurement can be done within a narrow range around the shifted position of the trailing edge. From this narrow range, a maximum level was selected to represent the far field sound pressure level. The range of the baseline measurement was from -30 mm to 30 mm with 5 mm increments from the shifted trailing edge. Whereas, for the serrated trailing edge measurement from -30 mm to 60 mm with the same increments from the shifted baseline trailing edge. Noise was measured for 20 s at a rate of 65 kHz, and a high-pass filter with a cut-off frequency of 500 Hz was applied in the data acquisition. The measured time series was converted in the frequency domain using the method of averaged periodogram with 50% overlap and Hanning window. The narrowband spectral resolution was 16 Hz. The background noise, the direction microphone system response function (assuming line source distributions) were corrected according to the method of Schlinker [24]. More details on the procedure can be found in Herr [25].

The microphone array consists of 96 *LinearX* 1/2" microphones arranged within a 1 m diameter circle. It was installed above the wind tunnel model facing the suction side. Noise was measured for 30 s at a sampling rate of 100 kHz. A high-pass filter with a cut-off frequency of 500 Hz was also applied in the data acquisition of the microphone array. The measurements were processed using CLEAN-SC [16] with removal of the diagonal component of the cross-spectral power matrix and Amiet's 2D shear layer correction. The spectra were calculated using the method of averaged periodogram with 0% overlap and rectangular windows. The narrowband spectral resolution was 24.4 Hz and the level is adjusted to a reference observer at a distance of 1 m from the sound source. In order to separate the trailing-edge noise from other noise sources, the post-processing was done for a localised area around the trailing edge with a span width of 0.4 m and a chord length of 0.16 m, and the sound pressure level is considered only for sound sources identified within this area.

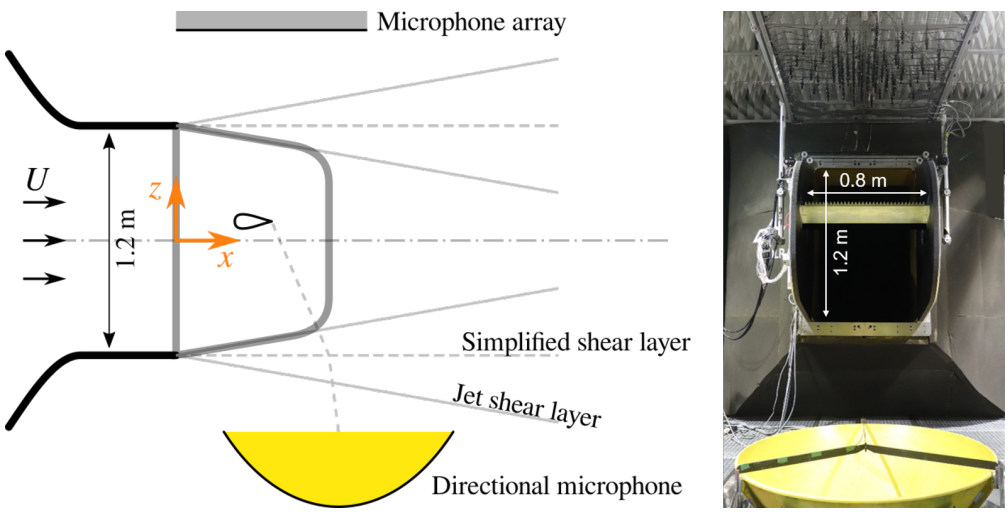

Fig. 6 AWB test set-up.

E. The NWB at Braunschweig

Aerodynamic measurements were performed in the closed test section of the Low-Speed Wind-Tunnel Braunschweig (NWB - *Niedergeschwindigkeitswindkanal Braunschweig*) of the German-Dutch Wind-Tunnels Foundation (DNW - *Deutsch-Niederländische Windkanäle*), see Fig. 7. The NWB is a closed-circuit low-speed wind tunnel that can be operated in a closed or open anechoic test section environment [26]. Its closed test section provides a cross-sectional area of 3.25 m × 2.8 m and a length of 8 m. Dedicated model extensions were built to extend the original HRM span to 2.8 m. Aerodynamic coefficients were derived from integration of the pressure distribution at midspan, cf. Section II. An additional wake rake with 135 total pressure probes (of 2.5 mm distance) and 7 static pressure probes was used on a high-resolution traversing system for drag measurements. Lift and drag polars were corrected for wall interference

according to the standard procedure by Garner et al. [21], thereby neglecting compressibility effects. Arrays of 10 G.R.A.S. 48LA 1/4" surface microphones in different layouts were also applied on the HRM in the closed test section. Necessary data corrections to account for the signal averaging over the sensing area of the microphones are currently being developed and validated pior to data release. Accordingly, the current paper is limited to the presentation of first aerodynamic test data. The results from a follow-up acoustic campaign in the NWB acoustic plenum (i.e. open-jet anechoic test environment) are not yet fully post-processed and will be subject of future work in this ongoing cooperation.

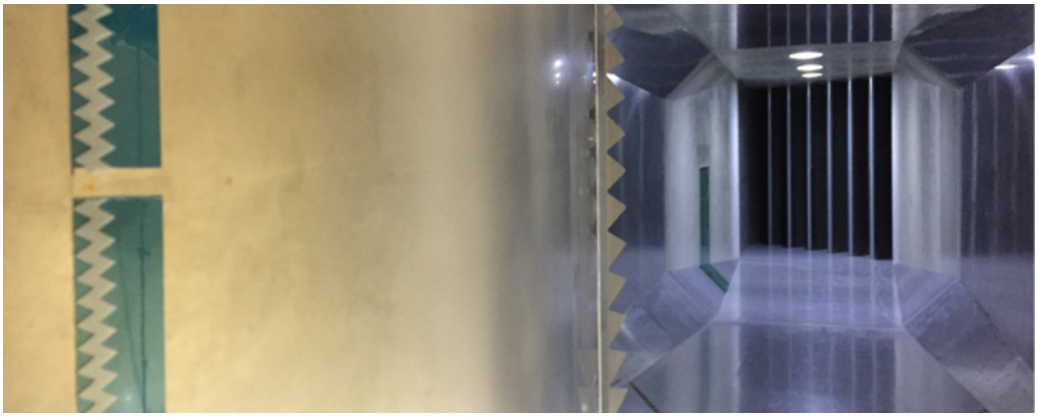

Fig. 7 NWB test set-up with tripping detail.

F. Facility summary

Table 1 provides an overview of the main characteristics of the wind tunnels used for this study. Note that the LTT and the NWB also have an aero-acoustic configuration (Kevlar panels and open-jet respectively), but aero-acoustic results from these facilities have not been used in this work.

Facility	**DTU**	**A-Tunnel** *Small/Large*	**LTT**	**AWB**	**NWB** *Closed*
Max. flow speed [m/s]	105	Small: 75 Large: 35	120	65	90
Test section [m]	3×2	S: 0.25×0.4 L: 0.7×0.4	1.8×1.25	1.2×0.8	3.25×2.8
Max. TI [%]	0.1	0.15	0.07	0.3	Long.: 0.06 Transv.: 0.15
Re_c measured ($\times 10^6$) [-]	1 - 4	S: 0.38 - 1 L: 0.18 - 0.46	1 - 3	0.38 - 0.77	1.9 - 4.8
Acoustic set-up	Kevlar walls	Open-jet	-	Open-jet	-
Aerodynamic set-up	Kevlar/Hard walls	Hard walls	Kevlar/Hard walls	Open-jet	Hard walls
Acoustic data	Mic. array, (CBF, Clean-SC)	Mic. array, (CBF)	-	Mic. array (Clean-SC) + Elliptic mirror	-
Boundary layer profiles	HWA	HWA	PIV	-	-
Airfoil model tested (span $\times$ chord [m])	HRM (2×0.9)	LRM (0.4×0.2)	HRM (1.25×0.9)	LRM (0.8×0.2)	HRM (2.8×0.9)
Model aspect ratio	2.22	2.00	1.39	4.00	3.11
Plot label	DTU	TUD-A-S TUD-A-L	TUD-LTT	AWB-MA AWB-EM	NWB
Plot colour	Green	Yellow Blue	Purple	Dark red Light red	Black

Table 1 Summary of the main characteristics and data retrieved from each facility.

IV. Aerodynamic Comparison

A brief aerodynamic comparison is given in this section. The lift and drag coefficients are presented in Subsection IV.A, where a comparison between tests with hard and Kevlar walls is also shown. The serrations effect on the lift curves is studied in Subsection IV.B, and finally the displacement thickness near the trailing edge is shown in Subsection IV.C.

A. Polar Curves

The lift coefficient measurements are presented in Fig. 8 for every facility, for both the clean and the tripped conditions. The C_l is obtained from the surface integral of the pressure coefficients C_p, measured by means of the surface pressure tabs described in Section II. Different wind tunnel corrections have been applied for each facility. For the A-Tunnel and the AWB measurements, which use open jet configuration, the effective angle of attack had to be corrected for distortions of the jet by the airfoil loading. A constant relation $\alpha_{eff} = K\alpha_{geo}$ was assumed, and the correction factor K was found by comparing the measured pressure distributions to XFOIL predictions [27]. The K values calculated from XFOIL were similar than the ones obtained from Brooks et al. analytical formula [28]. For the NWB, the LTT, and the DTU measurements with hard walls, the standard wind tunnel corrections according to Garner et al. have been applied [21]. DTU's Paul La Cour Tunnel measurements taken with Kevlar walls have been corrected using the methodology explained in Devenport et al. [15, 29], which is based on potential flow methods that take into account the wall presence including the flow transpiration through the Kevlar membranes. Details of this correction and a validation with Virginia Techical Unveristy can be found in the study of Fischer et al. [12]. The different nature of these corrections is represented in the polar plots, since using XFOIL for the corrections leads to the results matching a pre-defined set of polars. The measures corrected with XFOIL are shown with empty markers, whereas the other

methods are plotted with filled markers.

In the LTT and the DTU campaigns, the aerodynamic coefficient have been measured with both hard walls and Kevlar walls. A comparison of such measurements is given in Fig. 10. In the rest of figures, the measurements taken with Kevlar walls have been used.

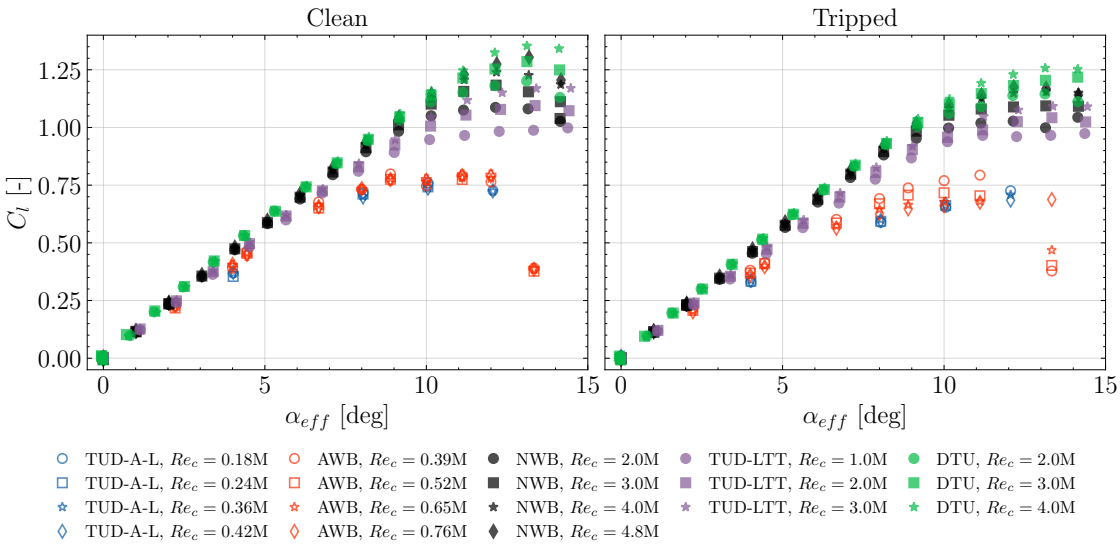

Fig. 8 Lift coefficient measured in the different facilities for a variety of Re_c numbers. Empty markers represent the measures corrected using XFOIL, and full markers indicate other correction methods.

The Reynolds number effect is clearly visible in Fig. 8. The measurements at the A-Tunnel and the AWB, at significantly lower Re_c than the other ones, show a reduced $C_{l,max}$ and an earlier onset of separation. There is a good agreement between both facilities with a slight difference in the slope in the linear region, which could be caused by the different aspect ratio in the tests (2 in the A-Tunnel, 4 in the AWB). A higher aspect ratio can lead to a increase in the lift coefficient slope [30]. The trend with Re_c in the stall region observed for the AWB measurements with tripped conditions appear to be the opposite as expected. The free transition point, as calculated with XFOIL, coincides with the position of the tripping device on the suction side. This possible interference is suspected as the source of such trend, but it has not been investigated further. A laminar separation bubble is observed for both the A-Tunnel and the AWB clean measurements, but it does not appear at higher Re_c. In the tripped case, the measured C_p are very similar and aligned with the XFOIL predictions. The C_p distributions are not shown here for conciseness. For the HRM results, a good agreement is observed specially between DTU and NWB, the former showing a slightly higher $C_{l,max}$ for the equivalent Re_c. This higher $C_{l,max}$ may be influenced by the use of Kevlar walls, as visible in Fig. 10. The LTT data has a lower slope which again could be attributed to a reduced aspect ratio and the pressure tabs not being in the middle of the test section. The different inflow turbulence of the tunnels could also play a role. Higher $C_{l,max}$ are measured in the clean cases, and the separation behaviour appears to be sensible to Re_c than in the tripped counterpart (except for the AWB as discussed above).

The drag coefficient results are shown in Fig. 9. All the data has been obtained from the momentum deficit in the wake using wake-rake measurements, as described in Section 7.2.3. of Russo [31]. As Re_c increases, C_d decreases, as seen very clearly by the difference between the models. In addition, larger drag values are observed in the tripped case compared to the clean measurements.

Fig. 10 compares the measurements in the LTT and the PLCT (DTU) for Kevlar and hard walls. The LTT data shows a very good agreement between both configurations at positive α_{eff}. However, a mismatch is observed at negative stall. The cause is an asymmetry in the test set-up with Kevlar walls. One side of the test section (facing suction side at $\alpha > 0$) was a Kevlar-Melamine panel with a solid back plate for noise absorption, whereas the opposite side was composed of a single Kevlar panel to allow for the acoustic measurements. Further details and consequences of the asymmetric permeability are explained in the study of Luesutthiviboon et al. [11]. DTU results also agree well, with the hard walls leading to a slightly lower $C_{l,max}$. The hard wall measurements were carried out with tripping at 5% in the suction side and 10% in the pressure side, unlike the Kevlar case, which was tested at symmetric 5% tripping. However,

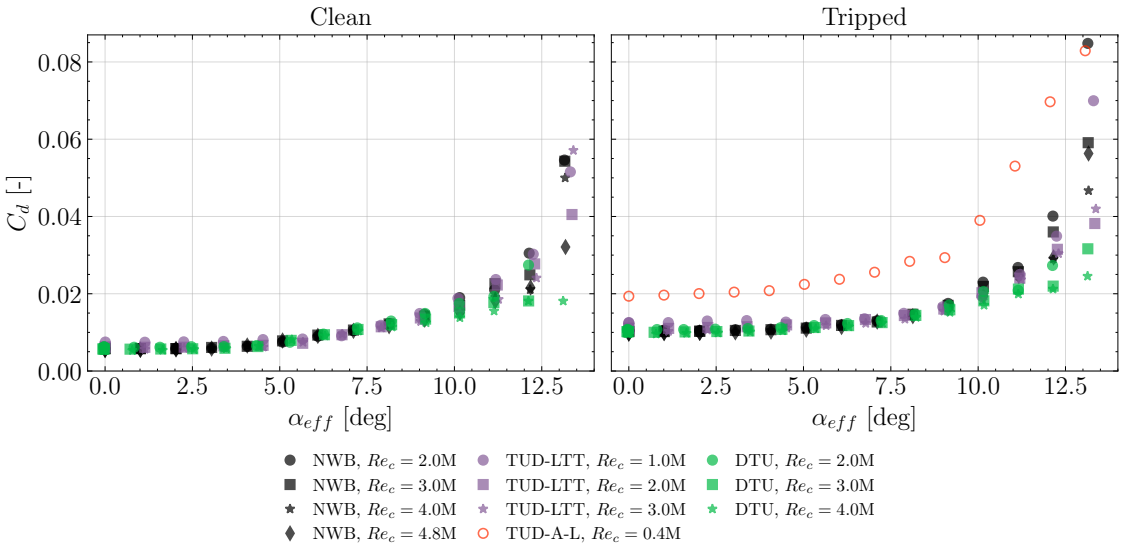

Fig. 9 Drag coefficient measured in the different facilities for a variety of Re_c numbers. Empty markers represent the measures corrected using XFOIL, and full markers indicate other correction methods.

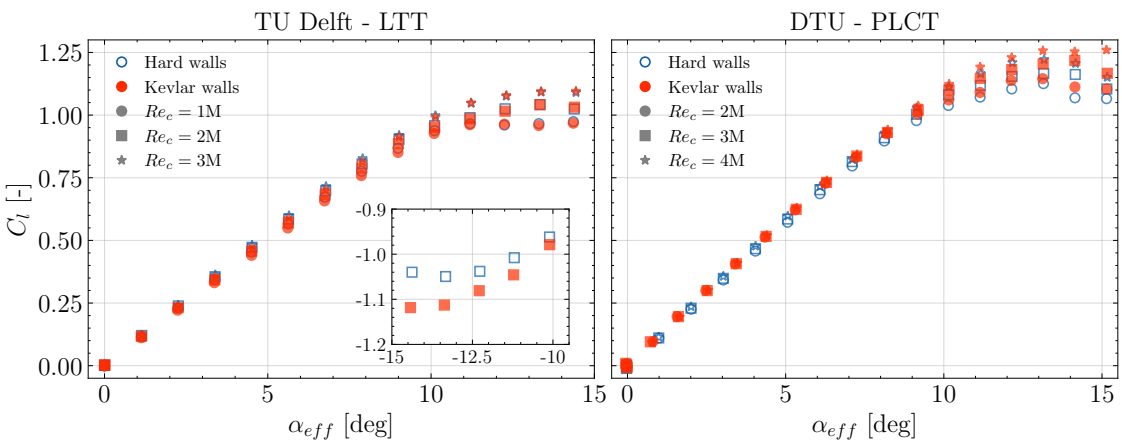

Fig. 10 Comparison of the lift coefficient curves measured in Kevlar and hard wall configurations at the Poul La Cour Tunnel (DTU) and the Low Turbulence Tunnel (LTT). The boundary layer was tripped in all the cases. Inner axis in the LTT plot shows negative stall behaviour.

it is considered that the trends appearing in the plot are the consequence of the different walls and not the tripping, since the same trends are found in the clean case.

B. Polar Curves - Serrations Effect

The serrations effect on the lift coefficient is presented in Fig. 11. The lift coefficient difference is calculated as $\Delta C_l = C_l - C_{l,ref.}$, where $C_{l,ref.}$ corresponds to the equivalent α_{eff} with straight trailing edge. Hence, positive ΔC_l values indicate increase in the lift coefficient when serrations are in place. The serrations installation in the HRM blocked the pressure tabs closest to the trailing-edge on both sides of the airfoil. Therefore, the results are not as accurate as in the baseline case, and are biased with respect to it. The general trends are still captured. Both geometries show positive ΔC_l because C_l has been calculated with the same reference chord but the serrations feature extended surface area. Higher ΔC_l is observed for iron serrations compared to the sawtooth ones, which is also attributed to a comparably larger surface area. The iron case also shows a higher sensibility with α_{eff}. Due to uncertainties in the installations the serration flap angles were higher than nominal in the DTU-PLCT tests ($\sim$ 4 deg.). It explains why the difference in ΔC_l

is larger than in the other tunnels. It is interesting to note that the same trends are also found in this case, but with an offset in ΔC_l.

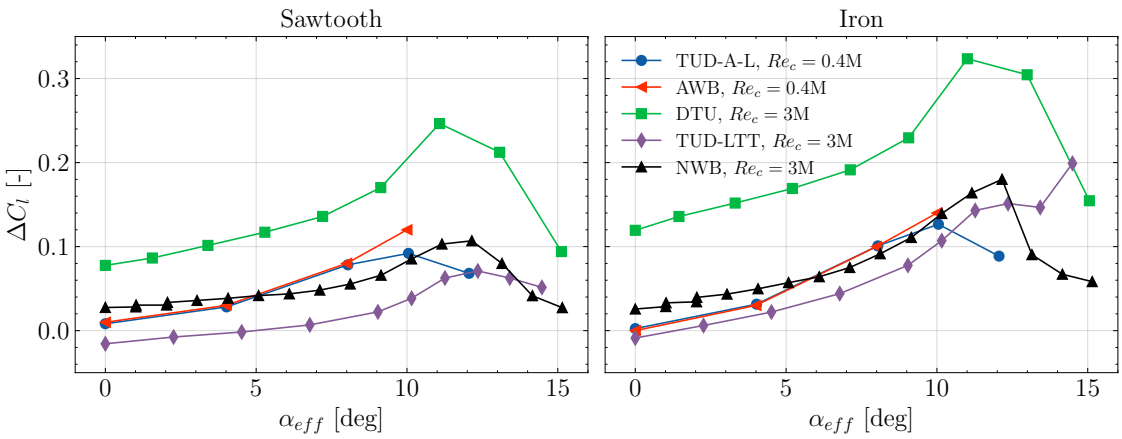

Fig. 11 Increase of lift coefficient with iron and sawtooth serrations measured at the different facilities. It was measured that DTU serrations were flapped 4 deg. instead of the nominal $\varphi = 0$ deg.

C. Displacement Thickness near the Trailing-Edge

The boundary-layer velocity profiles in the vicinity of the trailing edge were measured. HWA was used in the PLCT (DTU) and in the A-Tunnel (TU Delft), and PIV was employed in the LTT (TU Delft). The HWA measurements were performed at $X/c = -0.02$. Once the velocity profiles were obtained, the boundary-layer parameters were extracted. The location of the boundary-layer thickness and the edge velocity were determined by the region were the velocity fluctuations became constant, and fitting of the logarithmic layer was employed [32]. The work of Luesutthiviboon et al. [11] describes in detail the results obtained at TU Delft.

The boundary-layer displacement thickness (δ^*) is of special interest. It will be the parameter chosen to represent the turbulence length scale when scaling the acoustic results in Section V.D, following the classic scaling of Brooks et al. [33]. The measurements are presented in Fig. 12 for $\alpha_{eff} = 0$ deg and straight trailing edge. The lines show the XFOIL predictions obtained with 250 panels and $N_{crit} = 9$. This amplification factor has been chosen after comparing the C_p predictions with the measurements. Dashed lines represent the predictions for the LRM, and solid lines the HRM ones (to account for the different Re_c/M_U relation). Great accordance with XFOIL is observed in the HRM measures. The discrepancies are larger in the LRM, likely a result of a lower measurement resolution near the wall due to a very thin boundary layer. XFOIL captures well the general trends in terms of Re_c and tripping effect. It will be used to calculate δ^* for the scaling of the acoustic results given the lack of data for the rest of test conditions.

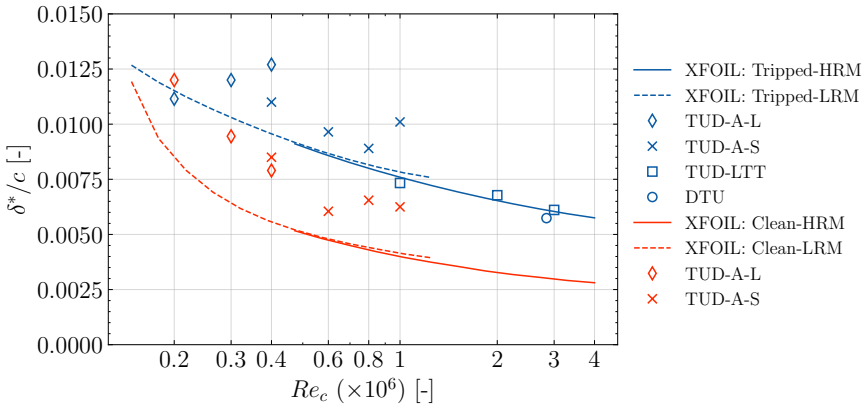

Fig. 12 Displacement thickness measured in the different facilities as a function of Re_c. Blue lines and markers correspond to the tripped boundary-layer conditions, whereas the clean cases are indicated with red.

V. Acoustic Comparison with Straight Trailing Edge

The far-field acoustic measurements with straight trailing-edge are compared in this Section. A summary of the data is firstly given in Fig. 13. The effect of the Reynolds number and the tripping is presented in Subsection V.A, the impact of the angle of attack is assessed in Subsection V.B, and the differences between facilities and measurement techniques are checked in Subsection V.C. Finally, the measurements are scaled together to the same conditions in Subsection V.D, and the collapse is studied. A reference pressure of 20 μPa is used to express the acoustic data with the Sound Pressure Level (SPL).

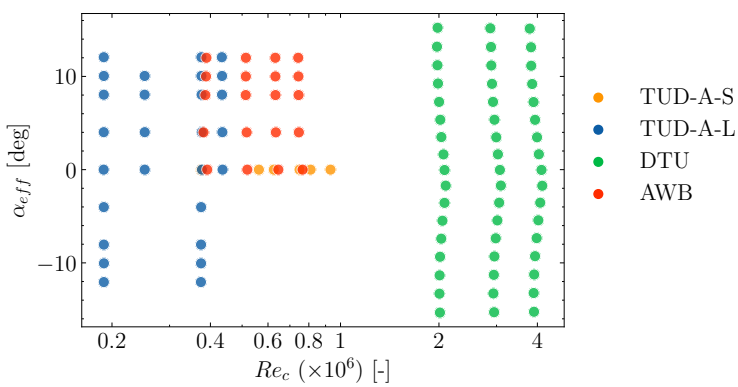

Fig. 13 Summary of the acoustic data for the baseline configuration with tripped boundary layer.

The broad Re_c range measured is shown in Fig. 13. The measurements carried out in the AWB and the A-Tunnel used the LRM, whereas the HRM was tested in the PLCT (DTU). In the lower Re_c range there are several overlapping points which allow for direct comparison between facilities. The geometrical angles of attack in the AWB and the A-Tunnel have been chosen such that their effective angle of attack are equivalent.

A. Effect of the Reynolds Number and the Tripping of the Boundary Layer

Fig. 14 presents the measured SPL in 1/3 octave bands in every facility for the straight trailing edge. Different Re_c numbers are presented together, and the tripped and clean cases are compared. All the results are normalised to a span width and an observer distance of 1m.

The forced transition effect is visible in all the facilities. The turbulent boundary layer arising from the tripping leads to a thicker δ^* than its clean counterpart, as shown in the HWA and PIV measurements presented in Fig. 12. This creates a noise increase in all the cases presented, which is found to be more important at low frequencies, and larger for increasing Re_c. The two lowest Re_c measured (0.19×10^6 and 0.25×10^6) are not following this pattern, and show larger $SPL_{1/3}$ for the clean case. The displacement thickness measurements shown in Fig. 12 indicate that δ^* may be

higher for the clean case at the lowest Reynolds numbers.

DTU measurements (Fig. 14b) and AWB measurements carried out with the elliptic mirror (Fig. 14d) show a high-frequency peak. The location of the peaks scales to very similar trailing-edge thickness based Strouhal numbers $St_{t_{TE}} = f t_{TE}/U$. This suggests that the cause of the peaks is trailing-edge bluntness noise [33]. The same phenomena would be also visible in the A-Tunnel and the array measurements in the AWB if the high frequency limit was larger. In the AWB case, the peaks are more clearly visible in the clean case. It could be explained by a major distortion of the vortex shedding from the turbulent boundary layer developed in the tripped case.

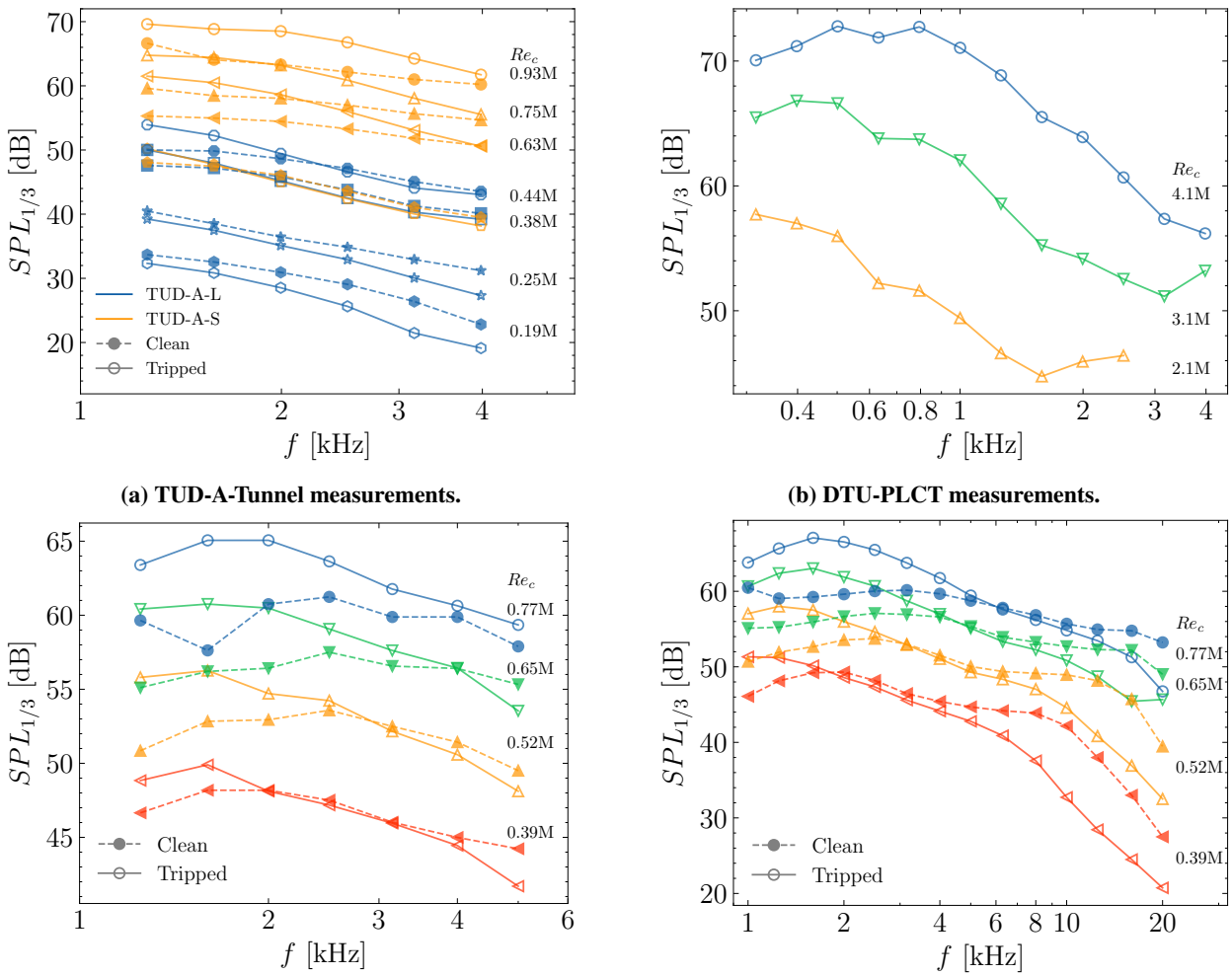

(a) TUD-A-Tunnel measurements.

(b) DTU-PLCT measurements.

(c) DLR-AWB measurements with microphone-array.

(d) DLR-AWB measurements with elliptic-mirror.

Fig. 14 Effect of the Reynolds number and the tripping in the trailing-edge noise measurements of the different facilities. Solid lines with empty markers represent the tripped conditions, and dashed lines with full markers indicate the clean equivalent.

B. Effect of the Angle of Attack

The acoustic polars, presented in Figs. 15 and 16, give a general overview of the angle of attack effect on the trailing-edge noise. The Overall Sound Pressure Level ($OSPL$) has been calculated from the 1/12 octave band spectrum, adding the bands between 1.2 kHz and 5 kHz. This range has been chosen since it contains the common f values for the LRM. These $OSPL$ values should only be analysed comparatively between the different cases to check that the trends are the same, but they do not represent the total $OSPL$ since the peak location of the spectrum is likely located at lower frequencies, specially for non-zero α_{eff}. To allow for similarity between different conditions, the $OSPL$ has

been scaled according to the classical law [33]:

$$OSPL_{scaled} = OSPL - 50\log_{10}(M_U/M_{ref}) - 10\log_{10}(\delta^*_{SS}/\delta^*_{ref}) - 10\log_{10}(b/b_{ref}) - 20\log_{10}(r_{ref}/r) \quad (1)$$

Where M_U is the Mach number based on the free-stream velocity, δ^*_{SS} is the boundary-layer thickness at the suction side, b is the span of the trailing edge, and r is the observer distance. The subscript $_{ref}$ indicates the reference quantities of the scaling, which are chosen as $M_{ref} = 0.13$, $\delta^*_{ref} = 0.008$ m, $b_{ref} = 1$ m, and $r_{ref} = 1$ m.

Fig. 15 compares the trends found in the LRM measures. A good alignment between facilities is observed. For the tripped conditions, the $OSPL$ decreases with α_{eff} and increases with Re_c. The effect of the angle of attack is attributed to the change introduced in the spectral shape: the level increases at low f and decreases at high f, and hence the frequency range selection for the $OSPL$ calculation determines the tendency. The change in the spectral shapes is further discussed in Fig. 17. The trend with Re_c could be explained similarly. The takeaway here is that it is consistent between facilities and with the qualitative expectations. The $OSPL$ at $Re_c \approx 0.4 \times 10^6$, the overlapping point for both facilities, agree within 2 dB. For the clean cases, the same trend with the angle of attack is observed except at $\alpha_{eff} = 8$ and 10 deg. In these cases, the presence of tones from laminar boundary layer instability noise lead to a $OSPL$ increase. These tones may be seen in Fig. 19, where the noise power spectral density is presented. There is also a good agreement in the Re_c at which this phenomena is observed.

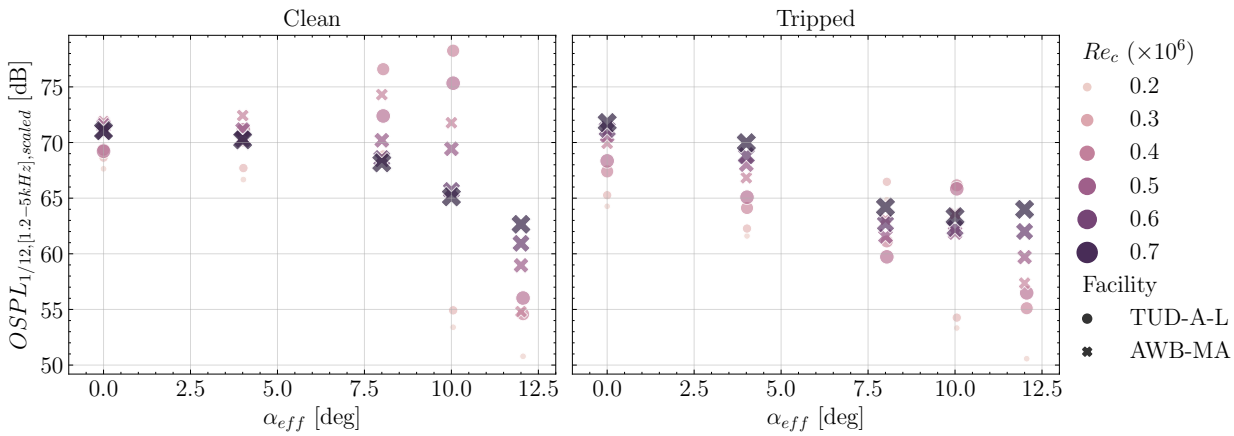

Fig. 15 Acoustic polars of the Low Reynolds number Model measured at A-Tunnel and the AWB for the baseline configuration and both tripped and clean boundary layer.

In Fig. 16 the acoustic polars measured at DTU for the tripped case are shown. The same trends with respect to the angle of attack and the Reynolds number are observed. In this case, the frequency range in the $OSPL$ calculations is 0.4 kHz to 5 kHz, since the Clean-SC post-processing allowed for a better resolution in the low frequency range. A Strouhal-based definition of the integration bounds would have allowed for direct comparison between the LRM and the HRM results. However, due to large Re_c range of the measurements, there is not enough overlapping part of the spectrum in the St space.

Fig. 17 shows the angle of attack effect on the spectra. Different α_{eff} are plotted together for the same Re_c for each facility. Both clean and tripped cases are presented. In the DTU measurements (Fig. 17b) a noise increase at lower frequencies is observed, accompanied by a noise reduction at higher frequencies. This is accredited to a thicker boundary layer developed in the suction side. In the other facilities only the noise reduction at high frequencies is observed due to the lack of low frequency data. From the AWB elliptic mirror data (Fig. 17d) the very high frequency results can also be studied. At $f > 8$–10 kHz, the levels increase again with the angle of attack. This could be attributed to higher energy content in the thinner pressure side boundary layer at these frequencies. The clean cases show the presence of tones at $\alpha_{eff} = 4$ and 8 deg, more clearly visible in the PSD plot shown in Fig. 19.

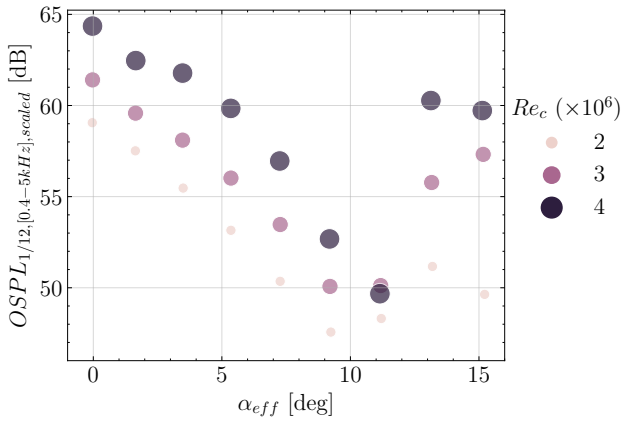

Fig. 16 Acoustic polars of the High Reynolds number Model measured at DTU-PLCT for the baseline configuration and tripped boundary layer.

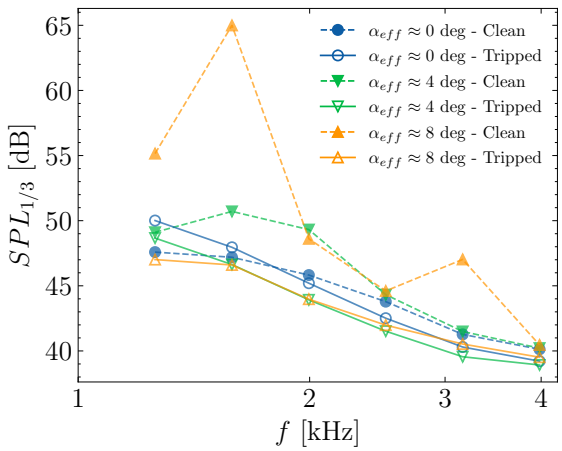

(a) TUD-A-Tunnel measurements at $Re \approx 0.38 \times 10^6$.

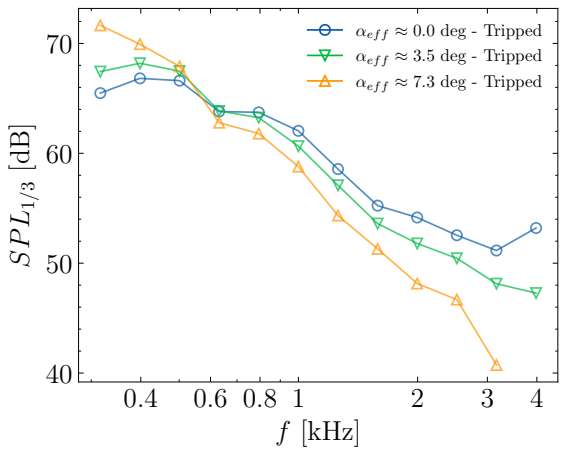

(b) DTU-PLCT measurements at $Re \approx 3 \times 10^6$.

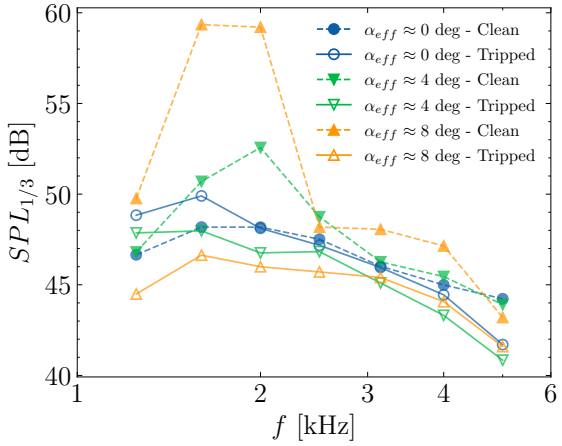

(c) DLR-AWB measurements with microphone-array at $Re \approx 0.39 \times 10^6$.

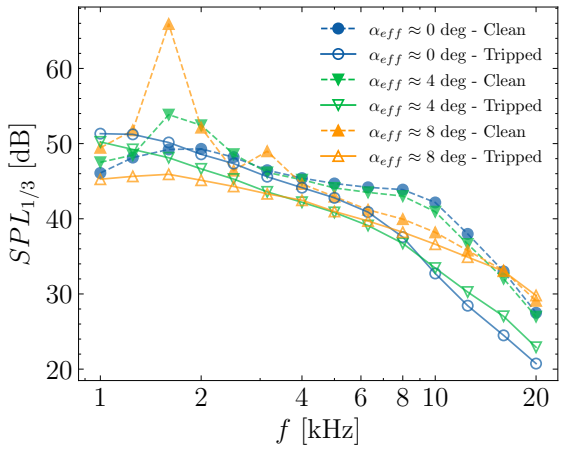

(d) DLR-AWB measurements with elliptic-mirror at $Re \approx 0.39 \times 10^6$.

Fig. 17 Effect of the angle of attack and the tripping in the trailing-edge noise measurements of the different facilities. Solid lines with empty markers represent the tripped conditions, and dashed lines with full markers indicate the clean equivalent.

C. Effect of the Facility and the Measurement Technique

The overlapping measurement point at $Re_c \approx 0.38 \times 10^6$ between the A-Tunnel and the AWB is now studied. The acoustic data is presented using the power spectral density.

In Fig. 18, the case at $\alpha_{eff} = 0$ deg shows a very good agreement between the two nozzles of the A-Tunnel. This allows both set-ups to be interpreted together in a continuous way. The two measurement techniques used in the AWB also collapse very well. Such results strengthen the consistency of the data. The peak levels of both facilities are virtually equal, but a mismatch in the spectral slope leads to deviations up to 6 dB at higher frequencies. There is still a difference in the post-processing used in each facility. It would be interesting to study the possible scatter introduced by using different beamforming algorithms, and establish a common post-processing method. Differences in the shear layer correction can also lead to a deviations in the spectral slope.

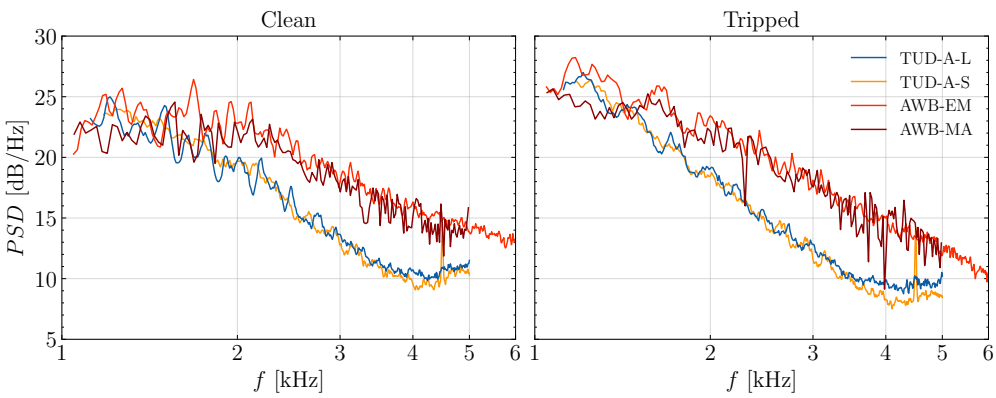

Fig. 18 Far-field noise power spectral density measured at the A-Tunnel and the AWB at 30 m/s for the baseline configuration with tripped boundary layer and $\alpha_{eff} = 0$ deg.

At $\alpha_{eff} = 8$ deg (Fig. 19), the presence of the laminar boundary-layer feedback-loop tones is clearly visible in the clean case. The small mismatch in the peaks location between the AWB and the A-Tunnel may correspond to deviations in the dynamic pressure or more likely to different development of the boundary layer attributed to the distinct aspect ratio, as observed previously in the small discrepancies in the polar curves (Fig. 8). Minor differences are also now observed between the elliptic mirror and the microphone array data from the AWB. The likely reason is the different directivities measured with each system, since the equipment are located at either side of the airfoil as depicted in Fig. 6. The elliptic mirror data will be taken for the subsequent comparisons. It does not only have a broader f range, but it is also consistent with the other facilities, which have the measurement system facing the pressure side of the airfoil when the model is pitched towards positive angles of attack.

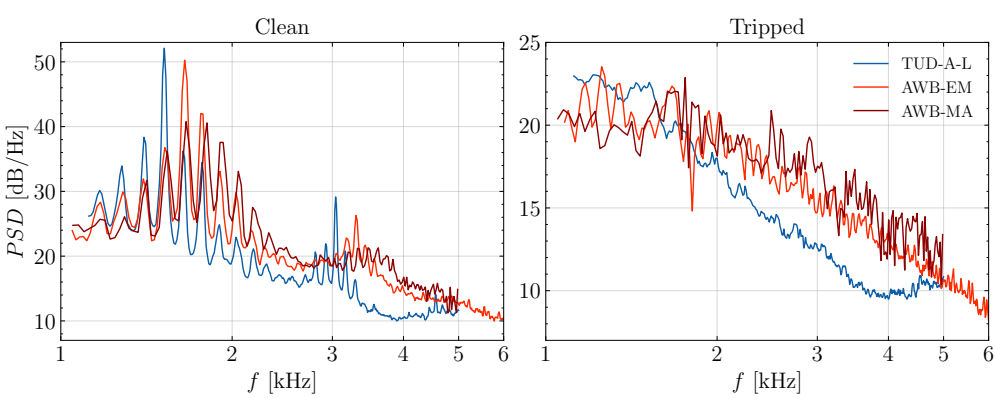

Fig. 19 Far-field noise power spectral density measured at the A-Tunnel and the AWB at 30 m/s for the baseline configuration with tripped boundary layer and $\alpha_{eff} \approx 8$ deg.

D. Scaling Study

This section studies the collapse of the scaling of the measurements performed at different Reynolds and Mach numbers. The classic scaling law has been applied [33]:

$$SPL_{scaled} = SPL - 50\log_{10}(M_U/M_{ref}) - 10\log_{10}(\delta^*_{SS}/\delta^*_{ref}) - 10\log_{10}(b/b_{ref}) - 20\log_{10}(r_{ref}/r) \quad (2)$$

Although this form of scaling is not expected to provide a perfect collapse in all the frequency range [34], it is the most widely used form, and it provides a useful first approach to compare and study the data. Only the forced transition cases are compared here, since the test conditions are more equivalent across the different facilities and the uncertainty is reduced. To have an estimate of the peak location of the measurements, the range of expected peaks $St_{\delta^*_{SS}}$ according to BPM [33] are plotted together with the measurements. Although the model was developed using a different airfoil and measurement techniques, it is depicted here as a rough reference to know where the peak frequency may lie.

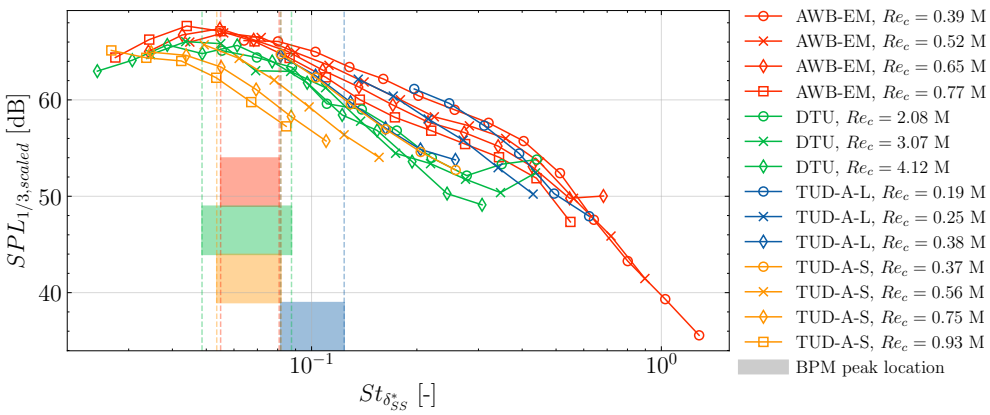

Fig. 20 Scaling of the measurements at different facilities for the tripped boundary layer case at $\alpha_{eff} = 0$ deg. The peak location predicted by the BPM model is also presented with vertical lines. Each colour covers the measurement range from the respective facility.

The scaled spectra at $\alpha_{eff} = 0$ deg. is presented in Fig. 20. According to the BPM predictions, the peak St_{δ^*} lies within the measured range. Good agreement in the peak locations and levels is observed between AWB and DTU despite deviations in the spectral slope. A trend with the Reynolds number is also observed: the curves shift to lower St_{δ^*} as Re_c increases. It is aligned with the BPM measurements, which estimated the peak St_{δ^*} as $St_{\delta^*} = 0.02M^{-0.6}$. This is particularly pronounced for the TUD results, which cover a much more extended peak Strouhal range than the corresponding BPM predictions. The mismatch between AWB and TUD, which encompass the same M_U and Re_c range, is not clear and should be investigated further. The effect of the different post-processing is suspected and should be assessed.

Fig. 21 shows the scaled spectrum at α_{eff} between 3 deg and 4 deg. The peak values agree well within 1.5 dB. As $St_{\delta^*_{SS}}$ increases, however, the collapse worsens and the scatter grows up to 10 dB. In that region, the same trend as the $\alpha_{eff} = 0$ deg is observed: within each facility, the lower the Re_c the higher the scaled SPL. This is specially visible for the two lower Re_c (0.19 and 0.25 million) measured in the A-Tunnel. The different Re_c may change the nature of the flow field and the behaviour of the boundary layer, which decreases the scaling collapse. This effect is found to be more important at the lower Re_c numbers. The large Re_c measurements performed at DTU escape this trend and show a more stable collapse.

The cases at α_{eff} between 7 deg and 8 deg are plotted in Fig. 22. The scatter between the DTU and the AWB results at low frequencies is larger in the preceding cases. Looking back at the lift curves (Fig. 8) it is observed how the loading difference is already important at this polar region. Different noise results are also expected in such a case. The better agreement between the A-Tunnel and the AWB, which polar curves are more alike, also supports this argument. The cases at $Re_c = 0.19 \times 10^6$ and 0.25×10^6 in the A-Tunnel are not shown in this plot, since the tripping effect was jeopardised by the location of the stagnation point, and laminar boundary-layer instability tones appeared.

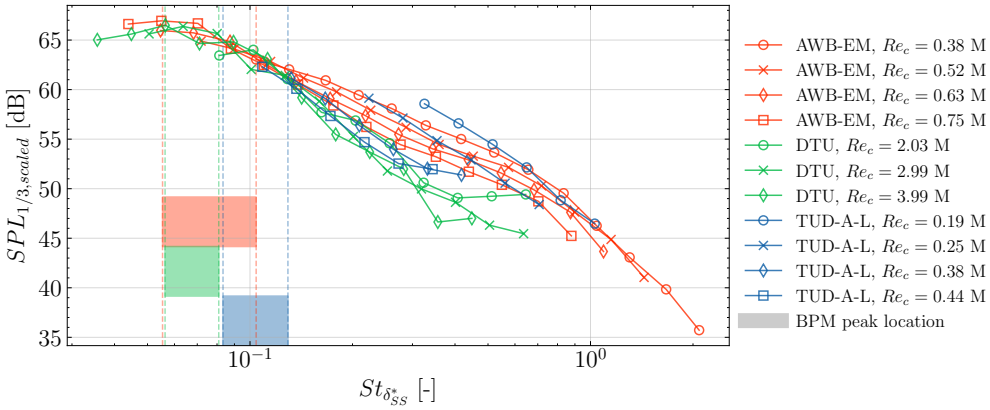

Fig. 21 Scaling of the measurements at different facilities for the tripped boundary layer case at $\alpha_{eff} \approx$ 3–4 deg. The peak location predicted by the BPM model is also presented with vertical lines. Each colour covers the measurement range from the respective facility.

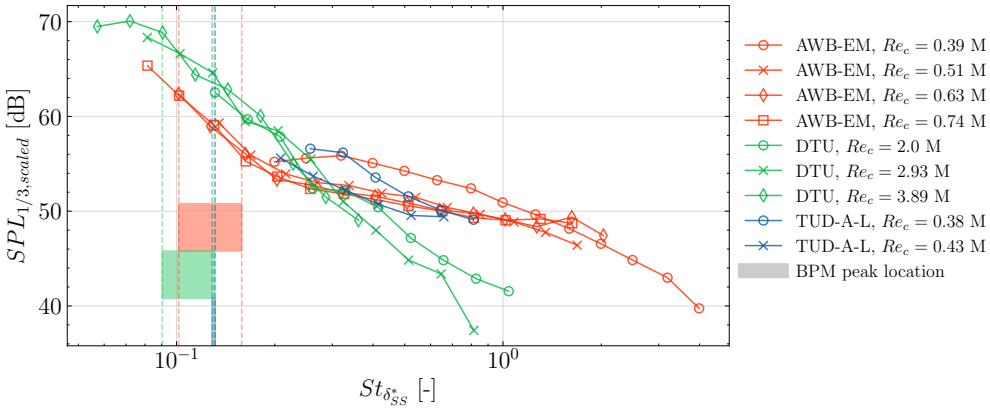

Fig. 22 Scaling of the measurements at different facilities for the tripped boundary layer case at $\alpha_{eff} \approx 7-8$ deg. The peak location predicted by the BPM model is also presented with vertical lines. Each colour covers the measurement range from the respective facility.

VI. Noise Reduction Comparison with Different Serrations

The effect of the noise reduction devices is studied in this Section. The noise reduction is calculated as $\Delta SPL_{1/3} = SPL_{1/3} - SPL_{1/3,\text{ ref.}}$, where the reference Sound Pressure Level $SPL_{1/3,\text{ ref.}}$ corresponds to the equivalent case with straight trailing edge at the same α_{eff} and Re_c. Therefore, negative $\Delta SPL_{1/3}$ indicate noise reduction. For this section, the DTU results have been post-processed with conventional frequency-domain beamforming instead of Clean-SC. The latter had convergence issues at low frequencies for the serrated cases, where the signal-to-noise ratio is lower. The CBF results show increased levels with respect to the Clean-SC equivalent [17], but this is acceptable in this section since the focus is on $\Delta SPL_{1/3}$.

$\Delta SPL_{1/3}$ is presented against $St_{\delta^*_{SS}}$ in Fig. 23 for the iron and sawtooth serrations without nominal flap angle. Only the tripped boundary layer cases are considered here. There is a fair scaling with $St_{\delta^*_{SS}}$, which supports previous results that showed that the noise reduction maximum depends on U [35, 36]. Two regions of noise reduction are identified for both serrations in the LRM results (AWB and TUD-A) The second noise reduction peak is similar to the results of P. Zhou et al. [37], which were also measured at similar Re_c number as the LRM. The HRM measurements (DTU) show two noise reduction regions in the sawtooth case, but only one in the iron case. The reason for the difference needs to be further investigated with additional measurements at high Reynolds number. At this point we cannot rule out that the noise reduction mechanisms behave differently at high Reynolds numbers. [37] found that this second peak was highly dependant on the serration flexibility and the flow alignment. The serration deformation was dependant not only on the stiffness and flow speed but also on the aerodynamic loading, which is directly related to the serration geometry. The

aerodynamic forces on the flap are much higher for the HRM compared to the LRM. Hence, it is possible that the flaps were subject to small scale vibrations due to the flexibility. Small scale vibrations could counteract the noise benefits in the high frequency range. Additionally, the iron shaped serrations have a larger surface area but the same thickness as the sawtooth serrations. Hence, the ratio of the aerodynamic forces to the flap stiffness is less favourable for the iron shaped serrations than the sawtooth serrations. The uncertainty in the serration flap angle could also play a role in the mismatch. In the first noise reduction peak, the iron serrations lead to a noise decrease up to 7.5-8 dB, whereas reductions up to 5 dB are seen for the sawtooth serrations. This is aligned with the computational studies by Avallone et al. [13].

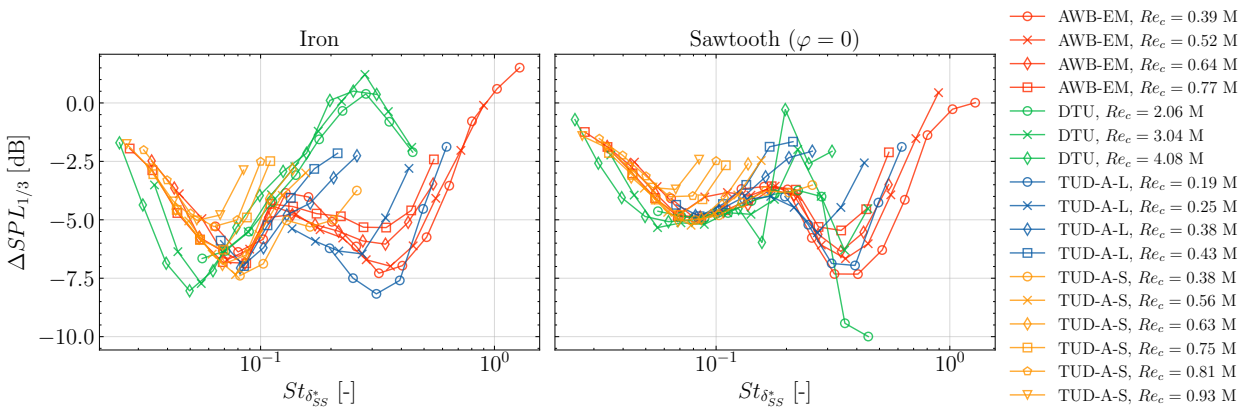

Fig. 23 Scaling of the $\Delta SPL_{1/3}$ with iron and sawtooth serrations with the displacement thickness based Strouhal number at $\alpha_{eff} = 0$ deg.

The cases with flapped serrations are shown in Fig. 24. Two noise reduction region are also identified here. The noise reduction maximum ($\sim$ 4 dB), however, is lower than in the preceding cases. This may be explained with appearing counter-rotating streamwise-oriented vortices in the serration edges when the airfoil is loaded [38, 39], since the airfoil is actually cambered when tested with flapped serrations.

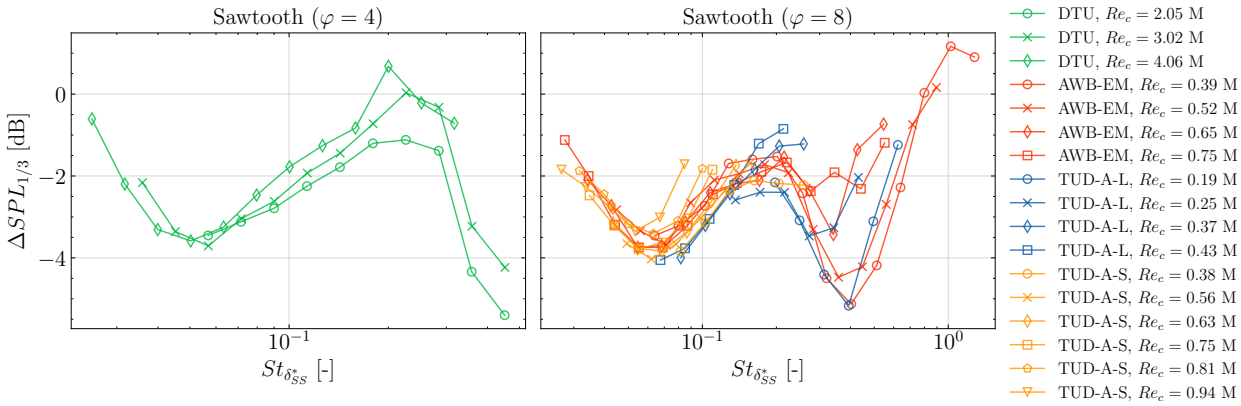

Fig. 24 Scaling of the $\Delta SPL_{1/3}$ with flapped sawtooth serrations with the displacement thickness based Strouhal number at $\alpha_{eff} = 0$ deg.

The effect of the angle of attack is summarised in Fig. 25. The $\Delta OSPL$ has been calculated for frequencies between 1200 and 5000 Hz for the LRM ($Re_c \approx 0.38 \times 10^6$), and between 400 and 3000 Hz for the HRM ($Re_c \approx 3 \times 10^6$). These values are arbitrarily chosen to have the best possible representation of the low frequencies, which drive the $OSPL$. Ideally, the same f or St range would have been chosen, but the present case is limited by the low SNR in the LRM results at low frequencies. Comparison between the models should be then analysed with care due to this difference. The noise reduction is presented for both the clean and the tripped cases. For the clean conditions, it is interesting to note the additional noise reduction measured at $\alpha_{eff} = 4$ and 8 deg. This noise decrease comes from the removal of the

laminar boundary-layer instability noise. It follows the study of [40], and it is attributed to bypass transition near the trailing edge that prevents separation, and removes the amplifier of the Tollmien-Schlichting waves.

For the tripped conditions, it is observed in the spectra (omitted for conciseness) that the angle of attack initially leads to a level increase at intermediate and high frequencies. This effect propagates to lower frequencies too when α_{eff} increases further, and it affects all the spectrum when stall is reached. This may be attributed again to the increasing airfoil loading, with the same reasoning explained previously for the flapped serrations. In Fig. 25 the Re_c effect is also observed. The earlier departure of the LRM cases from the attached polar region leads to noise increases at lower α_{eff} than in the HRM results. The larger slope observed for the iron serrations shows again a higher sensibility to the aerodynamic loading due to the increased surface area, as seen previously in the lift coefficient measurements (Fig. 11).

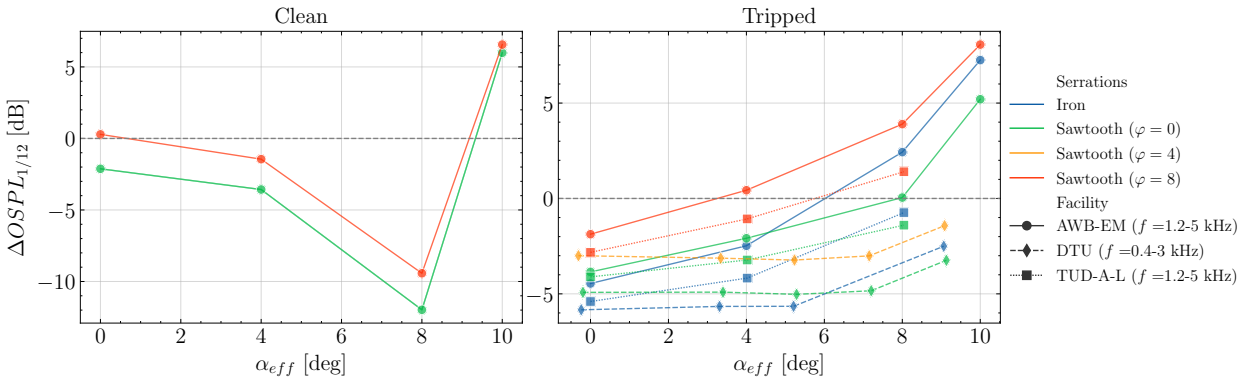

Fig. 25 Overall Sound Pressure Level as a function of the angle of attack and the serration type. LRM data (AWB-EM and TUD-A-L) measured at $Re_c \approx 0.38 \times 10^6$, and HRM data (DTU) at $Re_c \approx 3 \times 10^6$. The frequency range for the calculation of the $OSPL_{1/12}$ is indicated in the facility legend.

VII. Conclusion

The aerodynamic and aero-acoustic characterisation of the NACA 63_3-018 has been presented in this paper. Two models of this airfoil have been built for such purpose, with chord lengths of 0.2 m and 0.9 m, and they have been measured in 5 different wind tunnels: the A-Tunnel and the LTT at TU Delft, the Poul La Cour Tunnel at DTU, and the AWB and the NWB at DLR. The Re_c of the measures ranges from 0.18×10^6 to 4.8×10^6. Multiple angles of attack have been tested. The models have been studied with tripped and clean boundary layer, and sawtooth and iron serrations have also been installed and measured in both models.

The aerodynamic coefficients have been presented for the clean and tripped configurations for different Re_c. Tripping the boundary layer leads to a decrease of $C_{l,max}$ and a lower Re_c sensitivity in the stall region. Increasing Re_c leads to an increase of $C_{l,max}$ for both the clean and tripped case. This effect is very visible between models. Slight deviations in the lift slope were attributed to different aspect ratios. The effect of using Kevlar or hard walls for the testing has been also assessed. Good agreement between both configurations was observed, except for the negative stall region in the LTT measurements, which is the consequence of asymmetries in the set-up. The effect of the serrations on the lift coefficient has also been studied. A higher ΔC_l was found for the iron serrations due to a larger surface area. However, the measurements with serrations contained significant uncertainties in the flap angle. This was specially important for the DTU case, which showed deviations of 4 deg with respect to the nominal value. The velocity profile in the vicinity of the trailing edge has been also measured. The boundary layer displacement thickness (δ^*) has been calculated and compared to XFOIL predictions, which agreed well in terms of Re_c and tripping trends.

The acoustic results have been firstly discussed for the straight trailing edge configuration. The effect of the tripping on the far-field noise has been assessed. Within the same Re_c measured, it was observed that the forced boundary layer lead to a level increase up to 5 dB in the low frequency part of the spectrum. This was related to the increase of δ^*. Broadband peaks in the high frequency part were found and attributed to trailing-edge bluntness noise. Increasing the angle of attack lead to a rise in the levels in the low frequency part of the spectrum, and a decrease in the high frequency part. This was also associated to the varying thickness of the boundary layer. For the clean configuration, laminar boundary-layer instability tones appeared at non-zero α_{eff}. They were found to be Re_c dependant, and good agreement on the tone presence and location between facilities was observed. An overlapping measurement point was available at

$Re_c \approx 0.38 \times 10^6$ between the A-Tunnel and the AWB. Good agreement at frequencies around 1-2 kHz was found, but differences in the spectral slope lead to a mismatch up to 6 dB at 3-4 kHz. Although the physical model tested was the same, the post-processing of the data was different, and it could have introduced some deviations. A study of the possible scatter introduced in this step is required. The scaling of the acoustic data showed a good agreement on the peak locations and levels, specially between AWB and DTU results. Generally, the curves shifted towards lower St_{δ^*} as Re_c increases. This was particularly pronounced in the TUD measurements, which covered a more extended peak Strouhal range than the AWB equivalent and the BPM predictions. The Re_c effect was particularly visible at $\alpha \approx 7 - 8$. At this angle the lift coefficients were already different due to early separation at low Re_c, and thus the acoustic results were also distinct for the two airfoil models.

The noise reduction effect has been measured and studied for the different serration types. Tones present in the clean measurements were significantly attenuated with the add-ons installed, leading to reductions in the $OSPL$ up to 10 dB. The noise reduction spectrum $\Delta SPL_{1/3}$ scaled fairly well with St_{δ^*}, and good agreement was found between different facilities and Re_c. Two noise reduction peaks were generally observed. The iron serrations were found to provide up to 7.5-8 dB of maximum noise reduction, whereas for the sawtooth serration it was around 5 dB. The overall sound reduction decreased with the flap angle and the angle of attack. This is likely a consequence of the increased aerodynamic loading and the appearance of counter-rotating vortices in the serration edges. The iron serrations were more sensible to α_{eff} changes due to a larger surface that lead to higher loading, as it was observed when comparing the ΔC_l.

Funding Sources

The current work is part of Task 39 "Quiet Wind Turbine Technology", an initiative within the Technology Cooperation Programme (TCP) by the International Energy Agency (IEA). The authors would like to thank the German Federal Ministry for Economic Affairs and Climate Action (BMWK) for supporting the operation of this task.
The authors would like to thank the Danish Energy Agency for funding the participation of the Technical University of Denmark in the IEA Task 39 under the programme "Energiteknologiske Udviklings- og Demonstrationsprogram (EUDP)", Journal number 134-21022.

Acknowledgments

Special thanks are due to Jorge Pereira Gomes for his valuable support during the NWB measurement campaigns. We would like to thank the wind tunnel engineers Jimmy S. Beckerlee and Sigurd B. Ildvedsen for conducting the experiments in the Poul La Cour wind Tunnel at the Technical University of Denmark.

References

[1] Howe, M. S., "A review of the theory of trailing edge noise," *Journal of Sound and Vibration*, Vol. 61, No. 3, 1978, pp. 437–465. https://doi.org/10.1016/0022-460X(78)90391-7.

[2] Lee, S., Ayton, L., Bertagnolio, F., Moreau, S., Chong, T. P., and Joseph, P., "Turbulent boundary layer trailing-edge noise: Theory, computation, experiment, and application," *Progress in Aerospace Sciences*, Vol. 126, 2021, p. 100737. https://doi.org/10.1016/J.PAEROSCI.2021.100737.

[3] Oerlemans, S., Sijtsma, P., and Méndez López, B., "Location and quantification of noise sources on a wind turbine," *Journal of Sound and Vibration*, Vol. 299, No. 4-5, 2007, pp. 869–883. https://doi.org/10.1016/j.jsv.2006.07.032.

[4] Herr, M., Bahr, C., and Kamzurraman, M., "Workshop Category 1: Trailing-Edge Noise. Problem Statement for the AIAA/CEAS Second Workshop on Benchmark Problems for Airframe Noise Computations (BANC-II)," 2012.

[5] Herr, M., and Kamruzzaman, M., "Benchmarking of trailing-edge noise computations - Outcome of the BANC-II workshop," *19th AIAA/CEAS Aeroacoustics Conference*, American Institute of Aeronautics and Astronautics, 2013. https://doi.org/10.2514/6.2013-2123.

[6] Herr, M., Ewert, R., Rautmann, C., Kamruzzaman, M., Bekiropoulos, D., Iob, A., Arina, R., Batten, P., Chakravarthy, S., and Bertagnolio, F., "Broadband trailing-edge noise predictions— overview of BANC-III results," *21st AIAA/CEAS Aeroacoustics Conference*, American Institute of Aeronautics and Astronautics, 2015. https://doi.org/10.2514/6.2015-2847.

[7] Oerlemans, S., and Schepers, J., "Prediction of wind turbine noise and validation against experiment," *International Journal of Aeroacoustics*, Vol. 8, No. 6, 2009, pp. 555–584. https://doi.org/10.1260/147547209789141489.

[8] Fischer, A., Bertagnolio, F., Shen, W. Z., and Madsen, J., "Noise model for serrated trailing edges compared to wind tunnel measurements," *Journal of Physics: Conference Series*, Vol. 753, IOP Publishing, 2016. https://doi.org/10.1088/1742-6596/753/2/022053.

[9] Ferret Gasch, O., Oerlemans, S., Faßmann, B. W., Herr, M., Bertagnolio, F., Fischer, A., Arnold, B., and Lutz, T., "Trailing edge noise prediction of wind turbine airfoils: A benchmark exercise," *25th AIAA/CEAS Aeroacoustics Conference*, American Institute of Aeronautics and Astronautics, 2019. https://doi.org/10.2514/6.2019-2675.

[10] Timmer, W. A., and Rooij, R. P. J. O. M. V., "Summary of the Delft University Wind Turbine Dedicated Airfoils," *41st AIAA Aerospace Sciences Meeting and Exhibit*, American Institute of Aeronautics and Astronautics, 2003. https://doi.org/10.2514/6.2003-352.

[11] Luesutthiviboon, S., Lima Pereira, L. T., Ragni, D., Avallone, F., and Snellen, M., "Aeroacoustic Benchmarking of Trailing-edge Noise from a NACA 63_3–018 Airfoil with Trailing-Edge Serrations," *Under review, AIAA Journal*, 2022.

[12] Fischer, A., Bak, C., Lylloff, O., Olsen, A. S., Mikkelsen, F., Ildvedsen, S. B., Beckerlee, J. S., Kuester, M., and Intaratep, N., "Cross validation of the aerodynamic and acoustic measurements in two Kevlar-walled wind tunnels," *Acccepted for publication in: Journal of Physics: Conference Series*, IOP Publishing, 2022.

[13] Avallone, F., van der Velden, W. C., and Ragni, D., "Benefits of curved serrations on broadband trailing-edge noise reduction," *Journal of Sound and Vibration*, Vol. 400, 2017, pp. 167–177. https://doi.org/10.1016/j.jsv.2017.04.007.

[14] Allen, H. J., and Vinceti, W. G., "Wall interference in a two-dimensional-flow wind tunnel with consideration of the effect of compressibility," Tech. rep., NACA, Ames Aeronautical Laboratory, Moffett Field, California, US, 1944.

[15] Devenport, W. J., Burdisso, R. A., Borgoltz, A., Ravetta, P. A., Barone, M. F., Brown, K. A., and Morton, M. A., "The Kevlar-walled anechoic wind tunnel," *Journal of Sound and Vibration*, Vol. 332, No. 17, 2013, pp. 3971–3991. https://doi.org/10.1016/j.jsv.2013.02.043.

[16] Sijtsma, P., "CLEAN based on spatial source coherence," *International Journal of Aeroacoustics*, Vol. 6, No. 4, 2007, pp. 357–374. https://doi.org/10.1260/147547207783359459.

[17] Lylloff, O., *Aeroacoustic wind tunnel tests*, DTU Wind Energy, PhD Thesis, 2020. https://doi.org/10.11581/dtu:00000102.

[18] Merino-Martínez, R., Rubio Carpio, A., Lima Pereira, L. T., van Herk, S., Avallone, F., Ragni, D., and Kotsonis, M., "Aeroacoustic design and characterization of the 3D-printed, open-jet, anechoic wind tunnel of Delft University of Technology," *Applied Acoustics*, Vol. 170, 2020. https://doi.org/10.1016/j.apacoust.2020.107504.

[19] Johnson, D. H., and Dudgeon, D. E., *Array Signal Processing: Concepts and Techniques*, Prentice Hall, 1993.

[20] Timmer, W., "Two-Dimensional Low-Reynolds Number Wind Tunnel Results for Airfoil NACA 0018," *Wind Engineering*, Vol. 32, No. 6, 2008, pp. 525–537. https://doi.org/10.1260/030952408787548848.

[21] Garner, H. C., Rogers, E. W. E., Acum, W. E. A., and Maskell, E. C., "Subsonic Wind Tunnel Wall Corrections," Tech. rep., AGARD, Paris, 1966.

[22] Pott-Pollenske, M., and Delfs, J., "Enhanced capabilities of the Aeroacoustic Wind Tunnel Braunschweig," *14th AIAA/CEAS Aeroacoustics Conference (29th AIAA Aeroacoustics Conference)*, American Institute of Aeronautics and Astronautics, 2008. https://doi.org/10.2514/6.2008-2910.

[23] Sen, R., "Interpretation of Acoustic Source Maps Made with an Elliptic-Mirror Directional Microphone System," *Aeroacoustics Conference*, 1996.

[24] Schlinker, R., "Airfoil Trailing Edge Noise Measurements with a Directional Microphone," *4th Aeroacoustics Conference*, American Institute of Aeronautics and Astronautics, Atlanta, GA, U.S.A., 1977. https://doi.org/10.2514/6.1977-1269.

[25] Herr, M., "Trailing-Edge Noise—Reduction Concepts and Saling Laws," *Dissertation, DLR Report ISRN DLR-FB-2013-32, ISSN 1434-8454*, 2013.

[26] Bergmann, A., "The Aeroacoustic Wind Tunnel DNW-NWB," *18th AIAA/CEAS Aeroacoustics Conference*, American Institute of Aeronautics and Astronautics, Colorado Springs, Colorado, USA, 2012. https://doi.org/10.2514/6.2012-2173.

[27] Drela, M., "XFOIL: An Analysis and Design System for Low Reynolds Number Airfoils," *Low Reynolds Number Aerodynamics*, edited by T. J. Mueller, Lecture Notes in Engineering, Springer, Berlin, Heidelberg, 1989, pp. 1–12. https://doi.org/10.1007/978-3-642-84010-4.

[28] Brooks, T. F., Marcolini, M. A., and Pope, D. S., "Airfoil trailing edge flow measurements and comparison with theory, incorporating open wind tunnel corrections," *AIAA/NASA 9th Aeroacoustics Conference*, American Institute of Aeronautics and Astronautics, 1984.

[29] Brown, K. A., *Understanding and exploiting wind tunnels with porous flexible walls for aerodynamic measurement*, Virginia Tech, PhD thesis, 2016.

[30] Kiefer, J., Miller, M. A., Hultmark, M., and Hansen, M. O., "Effects of finite aspect ratio on wind turbine airfoil measurements," *Journal of Physics: Conference Series*, Vol. 753, No. 2, 2016. https://doi.org/10.1088/1742-6596/753/2/022040.

[31] Russo, G. P., *Aerodynamic measurements. From phyisical principles to turnkey instrumentation*, Woodhead Publishing, Cambridge, UK, 2011. https://doi.org/10.1533/9780857093688.

[32] Clauser, F. H., "The Turbulent Boundary Layer," *Advances in Applied Mechanics*, Vol. 4, No. C, 1956, pp. 1–51. https://doi.org/10.1016/S0065-2156(08)70370-3.

[33] Brooks, T. F., Pope, D. S., and Marcolini, M. A., "Airfoil Self-Noise and Prediction," Tech. rep., NASA, Hampton, VA, 1989.

[34] Herr, M., Appel, C., Dierke, J., and Ewert, R., "Trailing-Edge Noise Data Quality Assessment for CAA Validation," *16th AIAA/CEAS Aeroacoustics Conference*, American Institute of Aeronautics and Astronautics, 2010. https://doi.org/10.2514/6.2010-3877.

[35] Gruber, M., Joseph, P. F., and Chong, T. P., "On the mechanisms of serrated airfoil trailing edge noise reduction," *17th AIAA/CEAS Aeroacoustics Conference (32nd AIAA Aeroacoustics Conference)*, American Institute of Aeronautics and Astronautics, 2011. https://doi.org/10.2514/6.2011-2781.

[36] Moreau, D. J., and Doolan, C. J., "Noise-reduction mechanism of a flat-plate serrated trailing edge," *AIAA Journal*, Vol. 51, No. 10, 2013, pp. 2513–2522. https://doi.org/10.2514/1.J052436.

[37] Zhou, P., Liu, Q., Zhong, S., Fang, Y., and Zhang, X., "A study of the effect of serration shape and flexibility on trailing edge noise," *Physics of Fluids*, Vol. 32, No. 12, 2020. https://doi.org/10.1063/5.0032774.

[38] Avallone, F., Pröbsting, S., and Ragni, D., "Three-dimensional flow field over a trailing-edge serration and implications on broadband noise," *Physics of Fluids*, Vol. 28, No. 11, 2016. https://doi.org/10.1063/1.4966633.

[39] Arce León, C., Merino-Martínez, R., Ragni, D., Avallone, F., Scarano, F., Pröbsting, S., Snellen, M., Simons, D. G., and Madsen, J., "Effect of trailing edge serration-flow misalignment on airfoil noise emissions," *Journal of Sound and Vibration*, Vol. 405, 2017, pp. 19–33. https://doi.org/10.1016/j.jsv.2017.05.035.

[40] Chong, T. P., and Joseph, P. F., "An experimental study of airfoil instability tonal noise with trailing edge serrations," *Journal of Sound and Vibration*, Vol. 332, No. 24, 2013, pp. 6335–6358. https://doi.org/10.1016/j.jsv.2013.06.033.